UNIVERSIDAD DE CONCEPCIÓN
FACULTAD DE CIENCIAS FÍSICAS Y MATEMÁTICAS
DEPARTAMENTO DE ASTRONOMÍA

FORMATION OF ULTRA-FAINT DWARF SPHEROIDAL GALAXIES: Ursa Major II, a collapsing scenario

FORMACIÓN DE GALAXIAS ENANAS ESFEROIDALES ULTRA DÉBILES: Ursa Mayor II, un escenario de colapso

Por: José Ignacio Vergara Landeros

Tesis presentada a la Facultad de Ciencias Físicas y Matemáticas de la Universidad de Concepción para optar al grado académico de Titulado en Astronomía.

Mayo 2024
Concepción, Chile

Profesor Guía: Dr. Michael Alois Dominik Fellhauer

To my family who always supported me. Haroldos, who were always there. Argos, who always knew how to make me laugh (Yeah, Mailo too). The bird girl, who cheer me up every time I needed it. Thank you.

Resumen

Las galaxias enanas esferoidales son el tipo de galaxia enana con luminosidad más baja encontradas alrededor de la Vía Láctea. Corresponden a los sistemas más antiguos y con mayor dominación de materia oscura conocidos, ofreciendo una oportunidad única de explorar la formación de las primeras galaxias y el comportamiento de la materia oscura en pequeñas escalas.

La formación de estos objetos es un debate en curso, mientras variedad de modelos intentan explicarlo, encuentran problemas con los escenarios de galaxias aisladas. Assmann et al. (2013) propuso un escenario para las enanas esferoidales, en donde cúmulos estelares se disuelven dentro de un halo de materia oscura. Luego, Aravena et al. (2019) adaptó este modelo para las enanas esferoidales débiles y ultra débiles, donde inicialmente las estrellas de la galaxia están distribuidas en un patrón fractal dentro del centro del halo de materia oscura, construyendo el componente luminoso débil observado.

Probamos un escenario de formación por colapso (no se encuentra en equilibrio virial) modelando la galaxia enana esferoidal ultra débil Ursa Mayor II a través de simulaciones numéricas utilizando el *Astrophysical Multipurpose Software Environment* (AMUSE), con las estrellas siguiendo una distribución fractal dentro de un halo de materia oscura que corresponde a una distribución de Plummer. Obtenemos un objeto de forma no esférica, cuyo tamaño depende completamente del radio del fractal inicial y solamente se volverá estable cuanto este radio sea mayor a la longitud de escala del halo de materia oscura. Para reproducir el radio de la mitad de la masa de Ursa Mayor II, necesitaríamos un radio fractal entre 350-450 pc. Obtuvimos dispersiones de velocidades mayores a la observada, dependiendo de ambos, el radio fractal y de Plummer.

Keywords – galaxia enana, materia oscura, fractal, Plummer

Abstract

The dwarf spheroidal galaxies are the lowest luminosity dwarf galaxies found around the Milky Way. They are the oldest and most dark matter-dominated systems known, offering an unique chance to explore the formation of the first galaxies and the behavior of dark matter on small scales.

The formation of these objects is an on-going debate, while several models try to explain it, they have problems with an isolated scenario. Assmann et al. (2013) proposed a scenario for dwarf spheroidals, where star clusters dissolve within a dark matter halo. Then, Aravena et al. (2019) adapted this model to faint and ultra-faint dwarf spheroidals, where initially the stars of the galaxy are distributed in a fractal pattern within the center of the dark matter halo, building the faint luminous component observed.

We tested a collapsing (non viral equilibrium) formation scenario modelling the ultra-faint dwarf spheroidal galaxy Ursa Major II by performing numerical simulations using the Astrophysical Multipurpose Software Environment (AMUSE), with the stars following a fractal distribution within a dark matter halo corresponding to a Plummer distribution. We obtain an object of non spherical shape, which size depends completely on the initial fractal radius and will become stable only when this radius is larger than the dark matter halo scale-length. To reproduce UMa II's half mass radius, we would need a fractal radius between 350-450 pc. We obtain velocity dispersions higher than observed, depending on both, fractal and Plummer radius.

Keywords – DM, UFD, collapsing scenario, fractal distribution, Plummer

Contents

List of Tables

List of Figures

Chapter 1

Theory

1.1 Dwarf Spheroidal Galaxies and their formation models

Dwarf spheroidal galaxies (dSph) are considered the basic building blocks of the galaxy formation process in the ΛCDM model. This type of galaxy is believed to be the most dark matter dominated systems, have the lowest stellar content and are poor in gas. There are different models that try to explain the origin of dSph galaxies, which can be separated by the different mechanisms that they consider. In the following four models, depending on three mechanisms are described.

1.1.1 Interaction between two or more galaxies

Some of these models are based on tidal and ram pressure stripping. Mayer et al. (2007) propose that the formation of dSph galaxies of the MW and Andromeda, specifically Draco, Ursa Minor and Andromeda IX; is attributed to the interaction between a dwarf irregular galaxy with rotational support and a host galaxy of MW scale. Also, all luminous galaxies should be surrounded by a few extremely dark-matter-dominated dwarf spheroidal satellites, and these should have the shortest orbital periods among dwarf spheroidals because they were accreted early (Mayer et al., 2007). Because gravity acts in the same manner on all forms of mass, it is expected that galaxies should contain a ratio of dark to ordinary luminous material roughly similar to the cosmic mean. However, dwarf spheroidals have much larger dark to luminous mass ratios, requiring some mechanism to

efficiently separate gas and stars from dark matter in order to explain their origin (D'Onghia et al., 2009). According to these models, dSph galaxies typically appear in proximity to spiral galaxies, but they do not account for the presence of distant isolated dSph galaxies.

In order to try to explain this isolated dSph galaxies D'Onghia et al. (2009) used a mechanism known as resonant stripping. They took in consideration that many nearby dwarf spheroidals lie in the same plane as the orbits of the Magellanic Clouds and the Magellanic Stream (D'Onghia et al., 2009). As this planar distribution is hard to explain if dwarf galaxies fall in individually, it can arise naturally if dwarfs become part of larger systems as members of groups of dwarfs, which have been found nearby. Also, it is expected that interactions between dwarfs would have been common in these environments, especially in the earlier stages of the Universe, when the Universe was younger and denser.

Interactions between dwarfs in a small group or between a dwarf and the forming Milky Way at high redshift are possible. Numerical experiments of encounters between dwarf galaxies can be seen in Figure 1.1.1. After nearly 2 billion years $\sim 80\%$ of the stars are stripped away from the smaller dwarf but its surrounding dark matter halo is less strongly affected, leading to a change in the ratio of dark to luminous matter (D'Onghia et al., 2009). This outcome, was especially rare because the stars reside in the deepest part of the potential well, making them the most tightly bound material in the galaxy. This result is caused by gravitational resonant stripping. Although resonances have previously been invoked to produce bridges and tails in collisions between galaxies of comparable mass, they found that resonant stripping can alter the mass to light ratio of dwarfs by removing luminous material more efficiently than dark matter, also it is most effective for galaxies interacting on prograde orbits, as in the example shown in the top panels in Figure 1.1.1

Resonant stripping is different from the other mechanisms with interaction between two or more galaxies, like tidal and ram pressure stripping. Because resonant stripping will affect gas and stars in a similar manner in a rotationally supported disk, it is simpler than models that require separate effects to strip the gas versus the stars (D'Onghia et al., 2009). This mechanism can also drive the morphological evolution of dwarfs. When operating in low mass groups, this mechanism can carry out pre-processing of dwarf galaxies by converting disk galaxies into spheroids

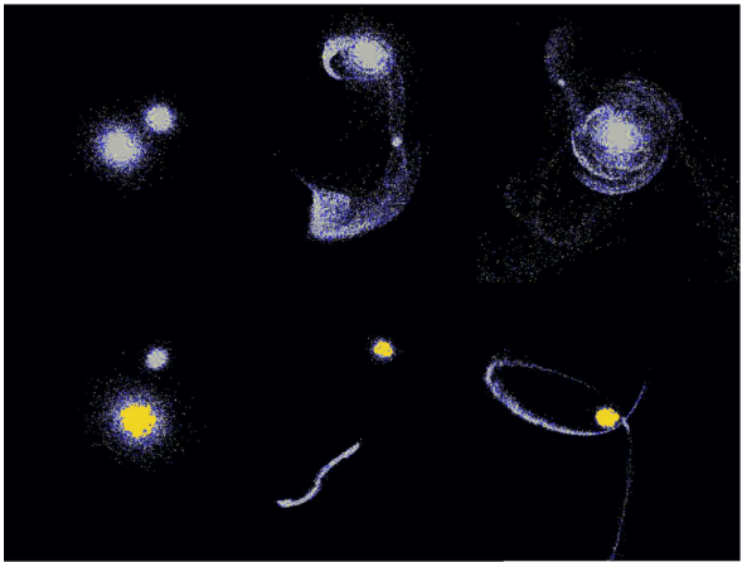

Figure 1.1.1: Encounters between galaxies through time. *Top row:* Interaction between a dwarf galaxy with a mass of $1.7 \times 10^8 M_\odot$ orbiting a larger dwarf with 100 times its mass. Only the stellar components are plotted. The upper left panel illustrates the initial set up where the two dwarfs approach one another on a prograde orbit. The upper middle panel gives the state of the system after 2 billion years, and the upper right panel shows the appearance of the galaxies after 7 billion years. If the galaxies have nearly the same mass they will merge quickly, masking the effects of resonant stripping because nearly all the luminous matter will remain bound to the remnant. *Bottom row:* The orbit of the same small galaxy (white) around the Milky Way today (yellow), which has 10,000 times its mass. Although the encounter is mostly prograde, the spin and orbital frequencies are no longer well-matched and the resonant response is suppressed. The left panel displays a region 150 kpc on a side and the initial setup; the middle and right panels show an expanded view 300 kpc on a side and give the state of the system after 2 and 7 billion years, respectively (D'Onghia et al., 2009).

before they are accreted by larger galaxies like the Milky Way. They found that dwarf spheroidal galaxies formed through this process exhibit properties that resemble to those of dwarfs observed in the Local Group. This model also predicts that dwarf spheroidals should have similar properties in different environments, which is supported by the observed similarities between dwarf spheroidals in the Perseus cluster and those in the Local Group. Now, this model gave a new possible formation process, however it still needs the interaction between the group of dwarfs or another galaxy.

1.1.2 Isolated Dwarf Galaxies

With the work of Sawala et al. (2009), a new posibility in the formation of dSph arrived. They modeled the formation and evolution of dwarf galaxies in fully cosmological, smoothed particle hydrodynamical (SPH) simulations. They simulate a cosmological volume with periodic boundary conditions, in which the haloes grow from small density perturbations imposed at high redshift. The initial conditions where chosen to reproduce galaxies of halo masses similar to the ones inferred for the Local Group dwarf spheroidals. The cosmological nature of their simulations allowed them to simultaneously follow the growth of the dark matter halo, and the evolution of the disipative component. Meanwhile, the full time evolution reveals the effect of the UV background, and let them compare with present day properties. Their numerical model includes cooling, star formation, chemical enrichment and feedback, and they allow for exchange of material with the intergalactic medium. They also include cosmological effects such as reionization (Sawala et al., 2009). This simulations resulted in the formation of galaxies similar to the dSph found in the Local Group. However, because of the limited initial conditions, they couldn't produce a system as luminous as Fornax, nor systems as faint as some of the ultra-faint dwarf galaxies.

They showed that feedback from supernovae and the cosmic UV background shape both the dynamical and the chemical evolution of dwarf spheroidal galaxies. As a result, these are inseparably linked, which is reflected in the scaling laws such as the mass-metallicity relation (Sawala et al., 2009). Also, that with choosing appropriate parameters it is possible to form systems similar to dwarf spheroidal galaxies in the Local Group, which means it is posible to replicate the diverse range of observed stellar masses and metallicities along with varying star formation histories, within a single evolutionary scenario and for a limited range of dynamical masses, as observed.

These simulations proved that gravitational potential is a critical value because of the combined effects of the supernova feedback and UV heating. Where both are necessary to reproduce the observations. In this case, a number of dynamical and stellar evolution effects conspire to reproduce the observed scaling relations. While all these effects undoubtedly play a role in the real systems, differing assembly and accretion histories, and differing environments are likely also to influence dwarf

spheroidal structure (Sawala et al., 2009).

This model has a problem. Where the density of the gas is sufficiently high they convert gas particles into star particles, having masses of about 10^2 to $10^3 M_\odot$. The problem appears because they didn't considered that those masses in stars form within an association or a small dissolving cluster, because it is below their resolution (Assmann et al., 2013). In addition they ignored the possibility that more massive star clusters could form through a single star-forming event.

1.1.3 Disolving Star Cluster Model

In 2013 Assmann et al. (2013) proposed a new formation scenario for dwarf spherical galaxies. In this scenario, the stellar populations of those galaxies came as a result of dissolving open clusters within a dark matter halo. The fiducial model is based on two widely accepted theories, the assumption that stars never form in isolation but in hierarchical structures, and the structure formation in the Λ-Cold Dark Matter (Λ-CDM) paradigm, where galaxies form hierarchically in the potential well of DM haloes and small haloes form first. They used the particle mesh code SUPERBOX (Fellhauer et al., 2000) where they considered the evolution of N = 30 star clusters within a dark matter halo with an NFW profile and then made four simulations, where three of them give rise to objects that resemble the observed dwarf spheroidal satellites of the MW without invoking external influences. One interesting result is that even after 10 Gyr of evolution sub-structure stemming from the formation process inside the dSph are still there. These substructures are mainly visible in velocity space, as can be seen in Figure 1.1.2, where the dynamics of the first realisation within 500 pc as two-dimensional pixel maps are shown. In the left panel the line-of-sight velocity dispersion is calculated for each pixel separately, here the high velocity dispersion in the center, but also at the locations where the off-centre density peaks are visible, which means that the DM cusp was able to erase most of the structure in positional space, but the structures in the velocity space survived. They called these structures "fossil remnants" . Because of these substructures, i.e. coherent motions, the measurements of the velocity dispersion of the object may be affected (Assmann et al., 2013). It's relevant to mention that one simulation is excluded , because this case presented a nucleus and around the Milky Way there is no such satellite dSph with one.

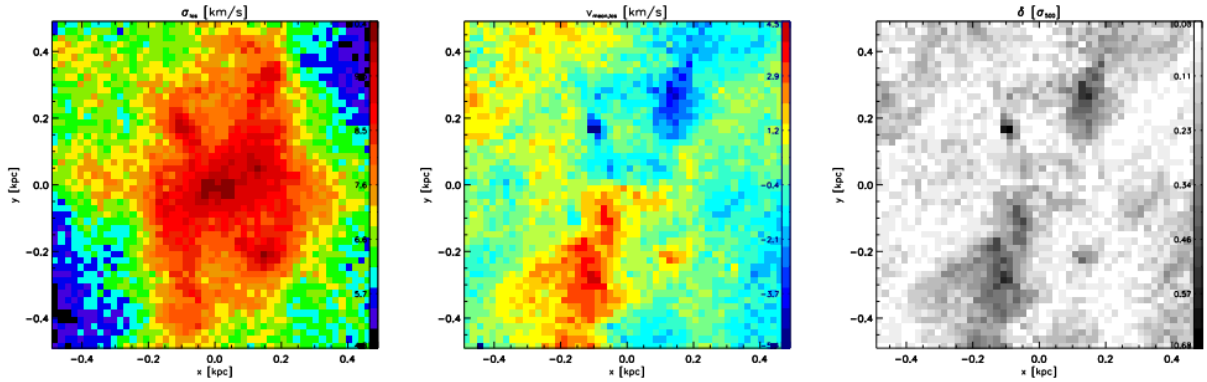

Figure 1.1.2: The 2D velocity structure of model 1. Shown is the central region out to 500 pc with a resolution of 20 pc per pixel. *Left*: is a map of the velocity dispersion measured in each pixel. *Middle*: shows the mean velocity map calculated for each pixel separately. *Right*: shows the scaled velocity deviation

In conclusion they proved that their model actually works. However, the sub-structures stemming from the formation process are only visible through the ultra-high particle resolution and at that time they were unobservable, as long as they cannot see all the stars of the dwarf. This model provide observers with predictions for future high-precision and high-resolution observations (Assmann et al., 2013). This observations arrived thanks to a specially developed algorithm called Beacon, which detect chemo-kinematical patterns in the observed and simulated data (Alarcón Jara et al., 2023). Here, they demonstrate that Leo I and Fornax probably originated from the superposition of different stellar components, rotating in the galaxy with projected angular momentum directed in different directions. Result that is in agreement with the dissolving star cluster model.

1.2 Faint and Ultra-Faint dSph galaxies

The satellite galaxies in the Milky Way with the lowest luminosity ($L < 10^5 L_\odot$) represent the lower limit of the luminosity function (Simon, 2019). These galaxies are the oldest, most metal poor, most dark matter dominated, and least chemically evolved stellar systems known. These are called ultra-faint dwarfs galaxies (UFdSph galaxies). Both observations and theoretical models indicate that UFdSphs formed at very high redshift, probably before the epoch of reionization. Unlike essentially all larger systems, they underwent little to no further evolution after that time, and have survived to the present day as pristine relics from the

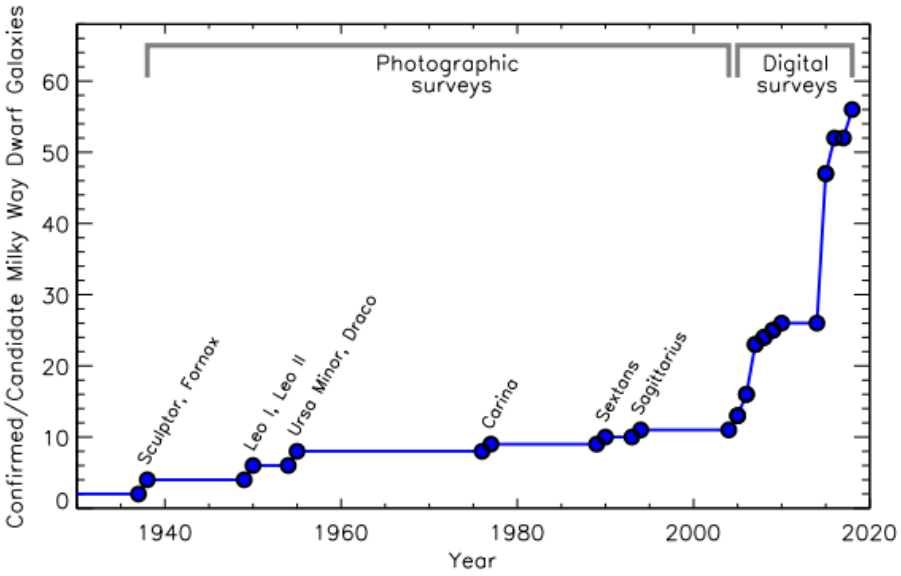

Figure 1.2.1: Milky Way dwarf satellite galaxies discovered over the years. The objects considered are all the spectroscopically confirmed dwarf galaxies as well as the suspected to be dwarfs, based on n less conclusive spectroscopic and photometric measurements (Simon, 2019). The two peaks in discoverings are due to SDSS (from 2005-2010) and DES/Pan-STARRS (2015)

early universe (Bovill and Ricotti, 2011). Because of these characteristic, they are an unique opportunity to study the formation of the first galaxies and the behavior of the dark matter on a small scale.

Since the first discovery of a faint dwarf galaxy, Sculptur by Shapley (1938), a lot of data became available, and the search for more dwarfs slowly revealed more dwarfs like the classical satellite galaxies of the Milky Way. The arrival of the Sloan Digital Sky Survey (SDSS) doubled the known population of Milky Way satellite galaxies (Figure 1.2.1)

Thanks to significant investments of telescope time in deep imaging and spectroscopy of the newly discovered objects, along with accompanying theoretical modeling, we now have a general understanding of the properties of these systems and their place in galaxy evolution and cosmology (Simon, 2019)

Why is it called faint or ultra faint instead of just a dwarf galaxy? Well, the dwarf galaxies known until 2005 have an absolute magnitude of $M_v = -8.7$ which is a V-band luminosity larger than $2.5 \times 10^5 L_\odot$ Their Plummer (half-light) radii are $\gtrsim$ 200 pc, and with the exception of Sextans and Ursa Minor, their central surface brightnesses are $<$ 26 mag arcsec^{-2}. In contrast, the dwarfs discovered in

SDSS and other modern surveys are up to a factor of $\sim$ 1000 less luminous, with half-light radii as small as $\sim$ 20 pc and surface brightnesses that can be $\sim$ 2-3 mag arcsec^{-2} fainter than that of Sextans (Bullock and Boylan-Kolchin, 2017).

1.2.1 Formation scenarios for UFdSph galaxies

The formation of UFdSph galaxies is an on-going debate, since the arrival of the SDSS the population of these galaxies has increased tremendously (as seen in Figure 1.2.1), also the development in technology has given more tools to analyze these structures in a more deeper way. Here I present the two formation scenarios for UFdSph galaxies that I've read, which are based on the previously mentioned ones for dSph galaxies.

1.2.1.1 Tidal stirring model

Łokas et al. (2012) investigated a possible formation scenario for UFdSph galaxies using the tidal stirring model as an explanation for the origin of dSph galaxies in the Local Group, method explained and proposed by Mayer et al. (2007) , which depends on the gravitational interaction between dwarf galaxies with initially disk-like structures and massive host galaxies. For the first time, they perform a series of tidal stirring simulations involving dwarf galaxies with disk-like structures embedded in DM halos with different inner density slopes, this by the use of collisionles N-body simulations.

They demostrated that the tidal stirring of disk-like dwarfs with a mass of $\sim 10^9 M_\odot$ over a period of $\sim$ 8Gyr can develop into the formation of stellar systems with characteristics similar to the UFdSph galaxies found in the vicinity of the MW. More specifically, their experiment showed that the production of those galaxies occurs when the initial disk-like dwarf progenitors are placed on relatively close, compact ($r_{peri} \lesssim 20$kpc), and eccentric ($r_{apo}/r_{peri} \gtrsim 5$) orbits within a host galaxy MW sized and are embedded in DM halos with a mild central density cusp ($\rho \propto r^{-0.6}$) (Łokas et al., 2012).

In their results, they also obtained UFdSphs with $M_V > -5$ mag, $\mu_V = 28 - 29$ mag arcsec^{-2} , and $r_{1/2} = 0.1 - 0.2$ kpc (Łokas et al., 2012). The resulting observational properties closely resemble those of UFdSph observed in the MW. This is valid for dwarf galaxies that have evolved on relatively compact orbits,

typically found within distances of 100 kpc from the center. However, even for these shallow density profiles, remnants resembling classical dSphs still emerge when the progenitors are on less compact orbits.

1.2.1.2 Fractal dissolving cluster model

Aravena et al. (2019) studied a new star formation scenario for UFdSph galaxies, based on the dissolving star cluster models for classical dSph galaxies (Assmann et al., 2013). In this formation scenario the stars are initially distributed in a fractal pattern within the center of the DM halo, which builds the faint luminous component observed in UFdSph. This scenario is simulated by using the Astrophysical Multipurpose Software Environment (AMUSE) and the direct N-body integrator ph4.

For the fractal distribution, they used the method proposed by Goodwin and Whitworth (2004). Here, the fractal is created within a cube of size 2 and positioning a "parent" in the center of the cube. Then, the cube is divided into N_{div}^3 equal sub-cubes and the first generations denominated as a "child" is placed at the center of each sub-cubes. In Aravena et al. (2019) study and in general is chosen $N_{div} = 2$ in which case there are 8 sub-cubes and 8 first-generation children. Now, the probability that a child matures and becomes a parent by own is N_{div}^{D-3}, where D is the fractal dimension and the value commonly used is $D = 1.6$. This process is repeated until there are more children than the required number of stars. The children are selected at random undergoing a culling process until the requeried number is left and the survivng children are identified with the stars of the cluster (Goodwin and Whitworth, 2004).

In their study they analized the UFdSph Segue 1, where they considered 700 particles in virial equilibrium with equal mass and a physical size $r_{fractal}$ of the system of 10, 30 and 50 pc. Also, they considered a background potential, specifically the Plummer Potential, and follow the evolution of the initial fractal distribution within an analytical halo for 5 Gyr.

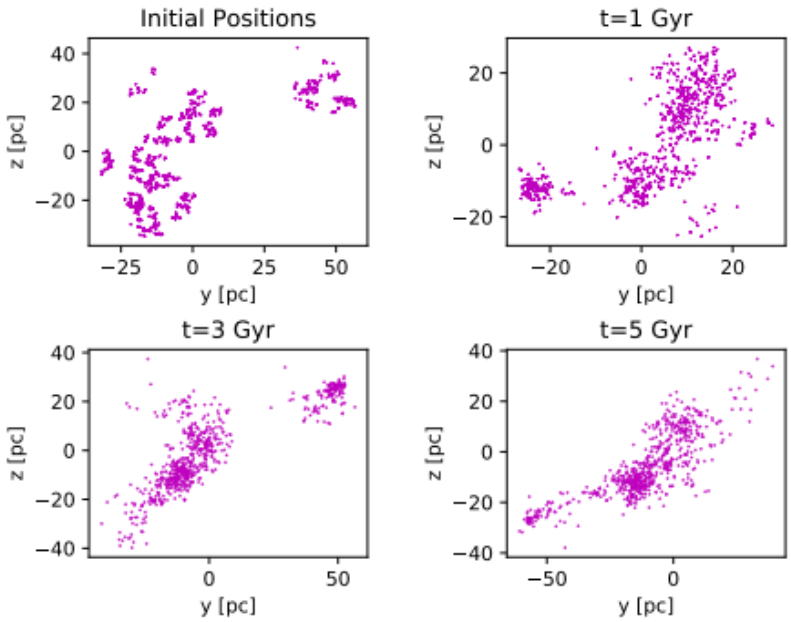

Figure 1.2.2: Evolution of the positions of the particles in the fractal distribution through the 5 Gyr of simulation. The pink dots are the 700 particles that were used, evolving in a $r_{fractal} = 50[pc]$. *Up Left*: First snapshot of the simulation at t=0, with the initial positions of the stars. *Up Right*: The simulation at 1 Gyr of evolution. *Down Left* The evolution of the distribution of the particles after 3 Gyr. *Down Right*: The last evolutionary stage of the simulation at 5 Gyr (Aravena et al., 2019).

In their results they came to the conclusion that the galaxy, even in the 5 Gyr of evolution, is still evolving as can bee sen in Figure 1.2.2. This final distribution of stars form a luminous object that resembles to an UFdSph galaxy like Segue 1. Also, the time-evolution of the Lagrangian radii for this distribution shows that 5 Gyrs is not enough for the Lagrangian radii to stay constant, as well for the effective radius of the galaxy, which is still to complex to study. Despite of the need to analyze the evolution of the galaxy for another 5 Gyrs, this study gave a visible result (Figure 1.2.2) that this formation scenario produces objects that have the distorted shapes of UFdSph intrinsically, without the need of an external influence (Aravena et al., 2019).

1.2.2 The Core-Cusp Problem

The study of early optical measurements of the rotational dynamics of late-type disk galaxies indicated a constant rotation velocity in their outer parts, which is also referred as flat rotation curves (Rubin et al., 1978). In these galaxies,

the gravitational influence of stars and gas alone can not fully explain de high rotation velocities observed in the outer regions, which would imply that most of the observed rotation must be due to another material, the DM. Although there are scenarios where this discrepancy could be explained by the stars alone, the arrival of observations using the 21-cm line of neutral hydrogen confirmed this mass discrepancy (Bosma, 1978).

The observed flat rotation curves indicate that the DM distribution in the outer regions of galaxies closely resembles that of an isothermal sphere, with a mass density profile of $\rho \sim r^{-2}$. Meanwhile, the rotation velocity associated with DM in the inner regions of disk galaxies show an approximately linear increase with radius. This uniform rotational pattern suggests the existence of a central core in the DM distribution extending across a significant fraction of the optical disk. While some researchers consider a non-singular isothermal sphere to describe this type of DM mass distribution, others lean towards a pseudo-isothermal sphere. Both of these models describe the data well (Kormendy and Freeman, 2004). Considering a pseudo-isothermal sphere (PI) sphere to represent the cored models, the mass distribution of this sphere is given by:

$$\rho_{PI}(r) = \frac{\rho_0}{1 + (r/R_C)^2}, \tag{1.2.1}$$

where ρ_0 correspond to the central density, and R_C is the core radious of the halo. This density distribution results in an asymptotic flat velocity V_∞ (de Blok, 2010).

Moving forward to the early 1990s, the first results of numerical N-body simulations of dark matter halos, following the CDM model, were released. However, these simulations did not replicate the core-like behavior observed in their inner regions. Instead, they were better represented by a steep power-law mass-density distribution known as a "cusp" (Navarro et al., 1996). In these simulations, the mass-distributions indicated an inner distribution $\rho \sim r^\alpha$ with $\alpha = -1$, where α represents the inner mass density power-law slope.

The value $\alpha = -1$ from the early CDM simulations contrasts with the expected value in the PI model, where a constant density core ($\rho \sim r^0$) implies $\alpha = 0$, this discrepancy is significant. With this it is possible to reach two very different description of DM distribution in galaxies.

In a dwarf galaxy the luminous component typically constitutes only a small fraction of the total mass within the luminous radius. Because of this, observations of the internal dynamics of these DM-dominated systems offer a direct probe into the inner regions of dark matter halos. Detailed rotation curve measurements from various dwarf galaxies indicate that the DM halo circular velocity increases nearly linearly with radius across their luminous regions. For spherical symmetry, this suggests the presence of a well-defined core in the halo, where the density of DM remains approximately constant, in the case of the "core" model ($\alpha = 0$) (Navarro et al., 1996). On the other hand, the "cusp" model ($\alpha = -1$) result in a DM density that rapidly increases, forming a "spiky" distribution toward the center, and has a rotation curve that increases as the square root of the radius (de Blok, 2010).

Figure 1.2.3 indicates that, with the exception of DDO 170 (*bottom right* panel) where observations provide poor constraints on the halo parameters, the CDM halos appear too concentrated to match the observations. In conclusion from this, while the cores of dwarf galaxies present a significant problem for CDM, the issue might not be as bad as previously assumed (Navarro et al., 1996), due to perturbations to the central regions of dwarf galaxy halos resulting perhaps from the sudden loss of a large fraction of baryonic material following intense star formation activity, can in principle reconcile the observations of dwarfs with the structure of CDM halos.

This problem can be summarized as the observational determinations tend to show slopes around $\alpha \sim 0$ while simulations tend to yield slopes around $\alpha \sim -1$. This persistent gap is known as the "The Core-Cusp Problem", also named as "the small-scale crisis in cosmology".

Using further modeling, de Blok et al. (2003) find that the rotation curves of Low Surface Brightness (LSB) galaxies and late-type, gas-rich dwarf galaxies indicate the presence of constant-density or mildy cuspy $\alpha \sim -0.2$ dark matter cores, this α value gives the best description of the data in the presence of realistic observational effects (de Blok, 2010). The most recent simulations continue to show resolved mass density slopes that are too steep to be easily reconciled with observations (typically $\alpha \sim -0.8$).Because of this, it remains a latent problem today.

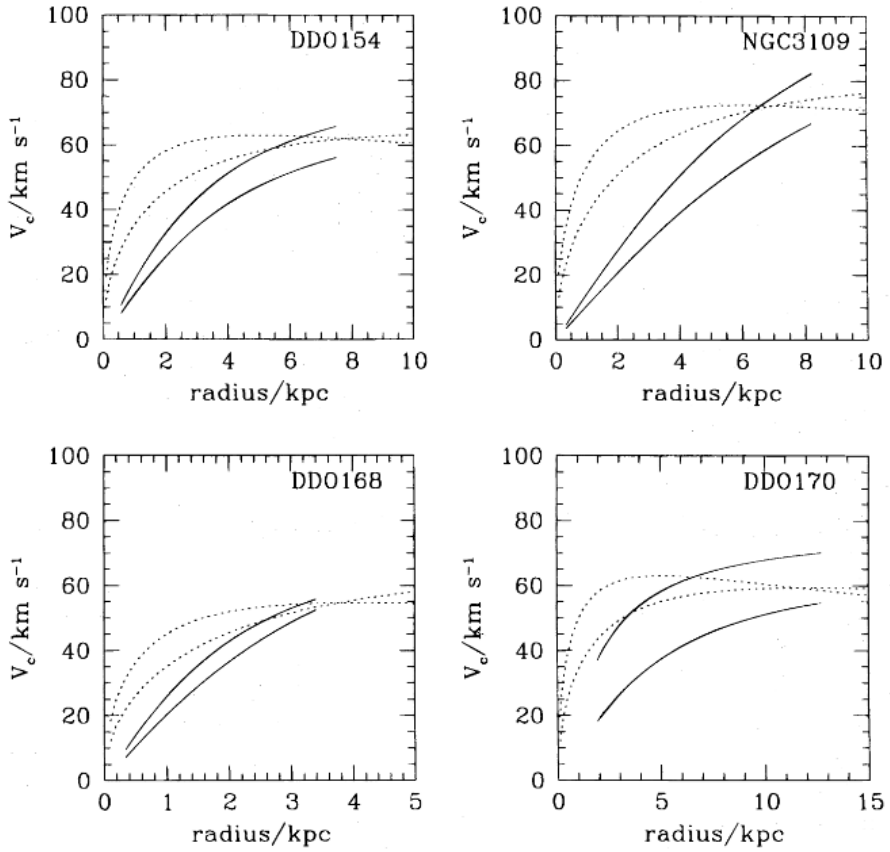

Figure 1.2.3: The contribution of the dark halo to the observed rotation curve of four dwarf galaxies (solid lines). The two curves are meant to encompass the halo contributions allowed by the observations and correspond to the results of assuming a "maximal disk" or a "maximal halo". These fit assume that the halo structure is of the form *Equation* 1.2.1 and are plotted only in the radial range in which the rotation curve is measured. The dotted lines in these plots are the expected contribution of a CDM DM halo, constrained to match the circular velocity at the outermost radius for which the rotation velocity has been measured. The two dotted lines are meant to represent the most and least concentrated halo compatible with this constraint.(Navarro et al., 1996)

The general nature of central densities also affects UFdSph galaxies, despite cuspy dwarf galaxies are also observed, it is often difficult to distinguish whether a given dSph is "cuspy" or "cored". Although, their halo mass and structure is potentially affected by the tidal interaction with the MW DM halo. In the context of host-satellite galaxy interactions, assuming identical orbital conditions, is less likely for UFdSph with more cuspy DM profiles to undergo tidal disruption, while a more cored profile has a smaller tidal radius and is more likely to be tidally disrupted and exhibit deformation in phase space (Peñarrubia et al., 2008).

Despite advances in observations and simulations providing us with more accurate measurements, it is still necessary to continue researching. In brief, investigations that incorporate the constraints and insights provided by the high-quality observations available, and that consistently describe and model the interactions between dark matter and baryons within a cosmological framework, are probably the most promising approach to resolving the core/cusp problem.

1.3 Characteristics

1.3.1 Stellar Kinematics

One of the first and more important steps to reveal the nature of UFdSph galaxies was the measurements of their velocity dispersions, which allowed to determine if they are gravitationally bound, dark matter dominated galaxies, or tidally disrupted systems (Simon and Geha, 2007).

The initial scpectropics observations of UFdSph were made for Ursa Major I and for Boötes I, resulting in a velocity disperion of $\sigma = 9.3^{+11.7}_{-1.2}$ km s^{-1} and $\sigma = 6.6 \pm 2.3$ km s^{-1}, with lumionsities of 9,600 and 21,900 $L_{\odot}$, respectively. If the stellar mass-to-light ratio is $\sim 2M_{\odot}/L_{\odot}$ (which is expected for an old stellar population with a standard IMF), then the expected velocity dispersions from the stellar mass alone would be $\lesssim 0.1$km s^{-1} (making use of the Wolf et al. (2010) mass estimator)(Simon, 2019). In both scenarios, the existence of a minimal velocity dispersion can be confidently excluded with high statistical significance, this proves that under standard assumptions UFdSphs cannot be exclusively composed of baryonic matter. After the spectroscopy analyses of the remaining UFdSphs, by the use of Deep Imaging Multi-Object Spectrograph (DEIMOS) on the Keck II

telescope, similar conclusions were reached.

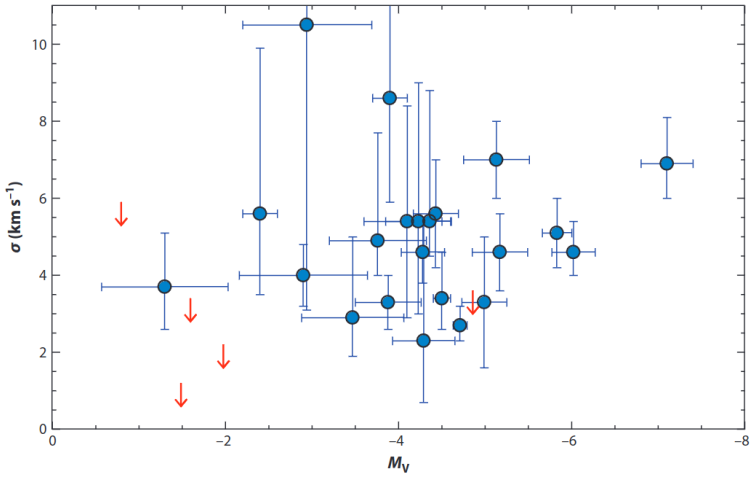

Figure 1.3.1: Line-of-sight velocity dispersions of ultra-faint Milky Way satellites as function of absolute magnitude. Measurements and uncertainties are shown as blue points with error bars, and 90% confidence upper limits are displayed as red arrows for systems without resolved velocity dispersions. Although there is a clear trend of decreasing velocity dispersion toward fainter dwarfs among the classical dwarf spheroidal galaxies, in the ultra-faint luminosity regime there is much more scatter, and any systematic trend is weak (Simon, 2019).

Simon (2019) plotted the velocity dispersion measurements of 27 out of 42 confirmed or candidate UFdSphs that were available at that time. These measurements are the observed dispersion of the radial velocities for a set of stars in each dwarf for which the spectra were obtained. To convert this velocity dispersions into dynamical masses, several assumptions are needed. After calculating the dynamical mass, the determination of dark matter content can be determined by comparing the stellar mass to the dynamical mass.

1.3.2 Metallicities

The metallicities of stars within UFdSphs galaxies are important for classifying them as galaxies as well for connecting them to the broader field of galaxy formation. Fortunately, the same spectra used to determine stellar kinematics can often yield measurements of metallicities. Recent advancements in spectral synthesis techniques allow for the determination of abundances of various elements beyond iron from medium-resolution spectra of stars within dwarf galaxies. Detailed chemical abundance patterns generally require observations at higher spectral resolution, which are challenging for dwarf galaxies due to the faintness of even

their brightest stars.

The first spectroscopic metallicity measurements for UFdSphs showed that these galaxies have very low metallicities ($[Fe/H] \lesssim -2$) and that the stars in each object span a range in metallicity. These studies were provided by Munoz et al. (2006), Martin et al. (2007) and Simon and Geha (2007). This characteristic set apart UFdSphs from globular clusters, as the star formation within these galaxies extended for a long period, enough for SN enrichment to occur, and that their gravitational pull is sufficiently strong to retain some of the supernova ejecta within the system.

These objects are interesting to study early chemical evolution and nucleosynthesis, because their small stellar masses imply that they have hosted relatively few SN explosions (Simon, 2019). Not only this, but also combined with their brief star-forming epochs, suggests that UFdSph could retain the unpolluted chemical signatures of small numbers of nucleosynthetic events (Bland-Hawthorn et al., 2010).

Simon and Geha (2007) proved that there exists a correlation between the stellar mass or luminosity of a galaxy and its mean metallicity in the UFD regime. Then, Kirby et al. (2013) quantified the Universal Stellar Mass-Stellar Metallicity Relation for Dwarf Galaxies (*Equation* 1.3.1), showing that a unified correlation applies to all types of dwarf galaxies across the Local Group.

$$[\mathrm{Fe/H}] = (-1.68 \pm 0.03) + (0.29 \pm 0.02) \log\left(\frac{L_V}{10^6 L_\odot}\right) \tag{1.3.1}$$

The existence of this correlation conflicts with severe tidal stripping of the stellar components of dwarf galaxies. Tidal stripping reduces the luminosity of a system while leaving its metallicity relatively unchanged. Because of this, stripping tends to increase the variance in the correlation. As this correlation remains in place, it sets an upper limit on the extent of stripping that could have occurred for the bulk of the dwarf galaxy population (Simon, 2019). However, given that the DM halos of galaxies extend far beyond their stellar components, a large fraction of the DM in dSph and UFDs could be extracted without affecting the luminosity-metallicity relationship .

In Figure 1.3.2 we can see that the scatter in the luminosity-metallicity relation

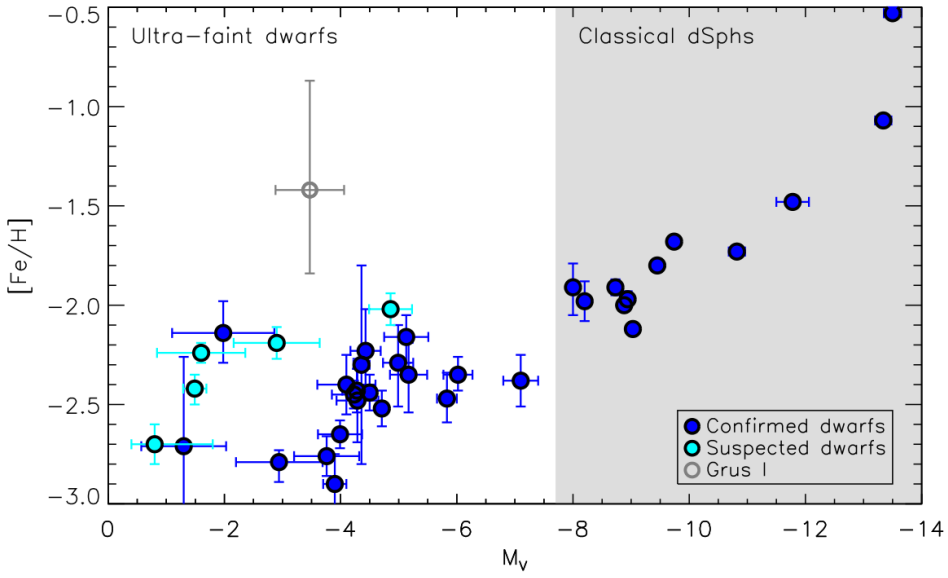

Figure 1.3.2: Mean stellar metallicities of Milky Way satellites as a function of absolute magnitude. Confirmed dwarf galaxies are displayed as dark blue filled circles, and objects suspected to be dwarf galaxies but for which the available data are not conclusive are shown as cyan filled circles. Grus I, for which there is no published classification, is shown as an open gray circle. The error bars in the vertical direction indicate the uncertainty on the mean metallicity of each object. The overall relationship between metallicity and luminosity is clear, although the scatter is large at the faint end (Simon, 2019).

seem to increase significantly for UFDs near to $M_V \gtrsim -5.5$, and even more at $M_V \gtrsim -4.0$. This increased dispersion can be considered as evidence that the UFdSph galaxies went through more stripping scenarios than the classical dSphs. But also, observational uncertities and errors may be responsible for some or all of the larger scatter at the lowest luminosities (Simon, 2019).

1.4 This work

Here, we study the formation of the UFdSph galaxy Ursa Major II, considering the formation scenario proposed by Assmann et al. (2013) and Aravena et al. (2019), which consist in an initial fractal distributed cluster within a DM halo which dissolves during its evolution. But with substantial differences from these two scenarios mentioned. In this project the initial velocities of the stars distributed in the fractal are equal to zero. This means that when the simulation starts, the particles will not have a random velocity, consequently they will be attracted to

the center of the cluster by gravity. This will generate a lot of close encounters between the stars and an interesting new way to see the formation scenarios for UFdSph. We follow their evolution for 1 Gyr. The simulations were ran by Astrophysical Multipurpose Software Environment (AMUSE).

This work is distributed as follow. In chapter 2 we describe AMUSE, the N-body simulator used and how we fixed the close encounters problem in our simulations. Chapter 3 shows the methodology, from the observational data of UMa II, to the initial conditions of the simulations, such as number of particles, fractal radius, mass of the DM halo and radius. In chapter 4 are shown the results from the simulations along with the respective analysis. Finally, in chapter 5 we summarize the conclusions of this work and what is expected to do in the future.

Chapter 2

Coding

2.0.1 Astrophysical Multipurpose Software Environment (AMUSE)

Astrophysical simulation has become an essential tool for comprehending the formation and evolution of astrophysical systems. The continuous advancement of computer hardware has increased the computational power available enormously, allowing codes to handle large realistic simulations and generate enormous amounts of data. However, when we talk about gravitational dynamics of hundreds of thousand of stars, the N-body code may not include algorithms for stellar evolution or the dynamics of the gas between the stars. The development of the latter requires a whole different set of expertise that may not be possessed by developers. Because of these requirements a very specific software environment is needed to simulate the formation scenario that I have to do.

To overcome this difficulties the open source Astrophysical Multipurpose Software Environment (AMUSE) was developed, by binding existing codes into a modern and flexible scripting language (Pelupessy et al., 2013) . AMUSE is an astrophysical implementation of the general principles of MUSE. It provides a unified interface and simplified access to astrophysical codes, enabling the execution of multi-physics simulations. The AMUSE project stipulates three basic functionalities:

1. A physically motivated and homogeneous interface for existing astronomical simulation codes.

2. The integration of multiple community codes from four fundamental areas

(stellar evolution, gravitational dynamics, hydrodynamics, and radiative transfer).

3. The capacity to create new simulation experiments by combining one or more of the community codes in diverse ways.

In this way, researchers can focus on physically relevant details, such as the calling sequence for different physical domains, without having to worry about the many technical details (Zwart and McMillan, 2018).

An AMUSE Python script dedicated to solving a specific problem prescribes the sequence of events and specifies the numerical solver that should be used to resolve each event. Once the initial conditions are generated and the simulation is concluded, the resulting data can be stored or then be analyzed by the use of the tools of AMUSE or custom tools developed by the user. The technical problems associated with coupling codes, setting boundary conditions, specifying run-time parameters, and guaranteeing that the various elements communicate in the proper units are entirely handled by AMUSE.

The user can select from a variety of gravitational N-body solvers (symplectic N-body codes, direct N-body codes, and tree codes) by changing a single word in the script. The same holds for stellar evolution codes (parameterized and Henyey codes), hydrodynamics solvers (smooth particle hydrodynamics and adaptive mesh refinement codes), and radiative transfer codes (Monte Carlo photon transport codes, and tessellated photon flow solvers) (Zwart and McMillan, 2018).

AMUSE encompasses various gravity codes that cover a wide range of dynamic regimes. Altought, the support for large scale cosmological simulations is limited. Fully relativistic metric solvers are also not included at present. However, several N-body integrators are available to use, such as Hermite0, PhiGRAPE, ph4 and HiGPUs ,which are direct N-body integrators with Hermite timestepping schemes, where the latter three are tooled to use hardware (GRAPE or GPU) accelerated force calculations (Pelupessy et al., 2013).

The interface to the different gravitational dynamics codes is the same and changing the core integrator in a script is trivial. However, the gravitational dynamics integrators that are included in AMUSE are geared towards different types of problem (Pelupessy et al., 2013).

2.0.1.1 ph4 integrator

The N-body simulator that will be used in my simulations is the ph4 integrator. The AMUSE ph4 dynamical module is a 4th order Hermite predictor-corrector N-body code written in C_{++} with block time steps and GPU acceleration. An N-body code is a piece of software that calculates the acceleration that a particle is subjected to, and updates its position and velocity. In the Hermite scheme higher (than individual time scheme) order derivates are used, in order to construct interpolation polynomials of the force (Makino and Aarseth, 1992).

In the Hermite individual timestep scheme (HITS), a particle defined as i, this particle has its own parameters defined as: time t_i, timestep Δt_i, position x_i and velocity v_i at the time t_i, and acceleration a_i and time derivative of acceleration $\dot{a}_i$ calculated at time t. The integration works in the following way:

1. The first step is select the particle i with a minimum $t_i + \Delta t_i$. Then, is set the global time t to be this minimum $t_i + \Delta t_i$
2. By using x, v, a and $\dot{a}$ it predicts the positions and the velocities of all particles at time t
3. Using the predicted positions and velocities it calculates the acceleration a_i and its time derivative $\dot{a}_i$ for particle i at time t
4. Calculate $a_i^{(1)}$ and $a_i^{(3)}$ using a Hermite interpolation using a and $\dot{a}$. Add corrections to the position and velocity of the particle i. Calculate the new timestep and update t_i.
5. Go back to step (1)

2.0.1.2 Bridge Method

For the analytic potential of the DM Halo, the bridge method is used. The Bridge scheme is a treedirect hybrid scheme that enables us to perform fully self-consistent N-body simulations of star clusters within their parent galaxies in a realistic time. Developed by Fujii et al. (2008), they consider a star cluster (subscript c) orbiting a parent galaxy (subscript g). The internal orbits of stars in the cluster are integrated using a fourth-order Hermite scheme (Makino and Aarseth, 1992) with direct summation of the interstellar gravitational forces. Interactions among the particles comprising the galaxy, and between galaxy particles and cluster stars, are

computed using a hierarchical tree force evaluation method (Zwart and McMillan, 2018).

Applied to the galaxy–cluster system, this scheme translates to the following algorithm (advancing from time "0" to time "1") (Fujii et al., 2008):

1. In this part of the process the velocities of cluster stars are adjusted by applying accelerations from the galaxy with time step $1/2\Delta t$. In a similar way, the velocities of galaxy particles are adjusted by applying accelerations from both the galaxy and the cluster with time step $1/2\Delta t$.

$$v'_c = v_{c0} + \frac{1}{2}\Delta t a_{g\to c0}, \tag{2.0.1}$$

$$v'_g = v_{g0} + \frac{1}{2}\Delta t a_{all\to g0} \tag{2.0.2}$$

2. The cluster positions and kicked velocites are updated (drift) with time step Δt, using the internal cluster integration scheme and kicked velocities, update galaxy particle positions with time step Δt using kicked velocities:

$$x_{c0} \to \text{(high-order scheme)} \to x_{cl}, \tag{2.0.3}$$

$$v'_c \to \text{(high-order scheme)} \to v_{cl}, \tag{2.0.4}$$

$$x_{gl} = x_{g0} + \Delta t v'_g \tag{2.0.5}$$

3. Recompute accelerations and complete the step by updating (kicking) all cluster and galaxy velocities:

$$v_{cl} = v'_{cl} + \frac{1}{2}\delta t a_{g\to cl}, \tag{2.0.6}$$

$$v'_{gl} = v_{gl} + \frac{1}{2}\Delta t a_{all\to gl} \tag{2.0.7}$$

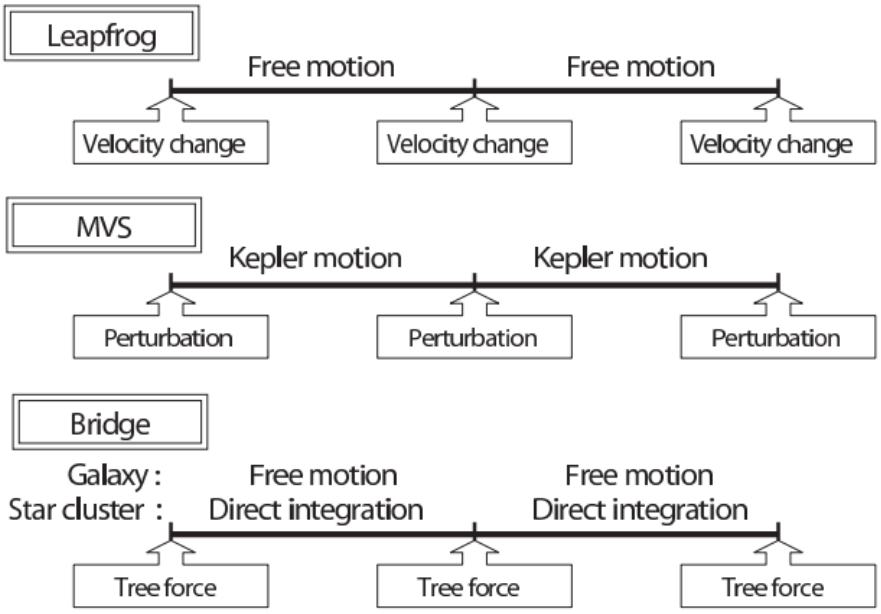

Figure 2.0.1: Algorith of the Bridge scheme. Figure by FUJII et al. (2007)

This basic scheme carries over to the generalized Bridge class in AMUSE (Zwart and McMillan, 2018), is summarized in the Figure 2.0.1.

2.0.1.3 Close encounters

The previously mentioned N-body integrators are designed to move large numbers of particles around a system, and are very efficient in doing so. However, in reality, many stars are born in a binary system or get a partner through dynamical interactions. In our particular case, as we will be working with bunch of stars that will find each other in the center, this situation will appear several times. In these circumstances, the short time steps associated with the tight orbits mean that errors start to mount and the integration effectively grinds to a halt once close binaries form (Zwart and McMillan, 2018). In our case, the code got stuck because of the close encounters, so a solution for the problem was needed.

In order to solve this situation and accordingly, in AMUSE, Zwart and McMillan (2018) depart from the N-body norm and adopt the Monte Carlo approach to multiple interactions. Thus, the AMUSE *multiples* package is designed to handle close encounters between stars and multiples in N-body systems

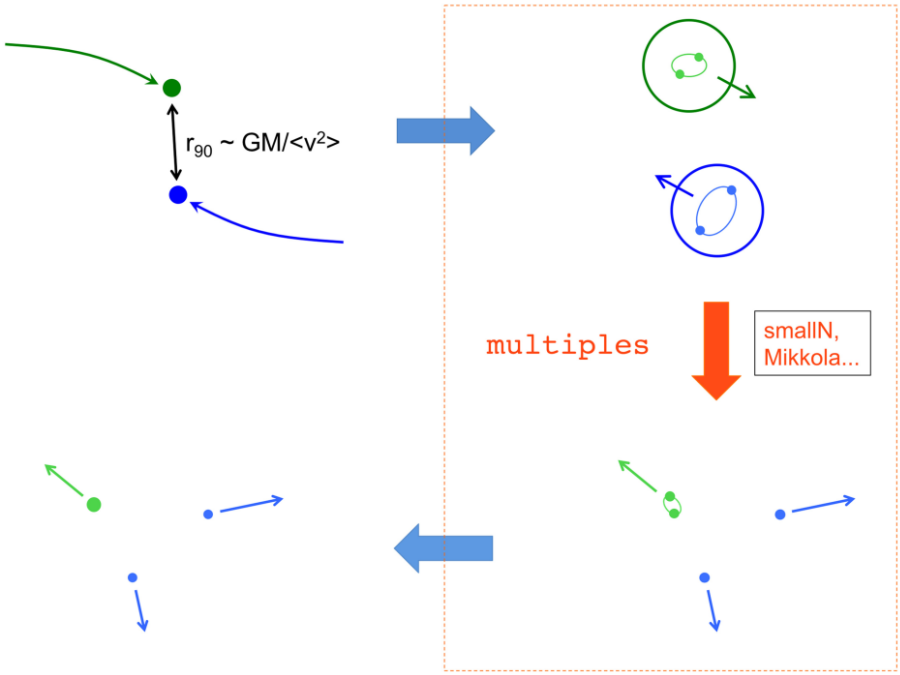

Figure 2.0.2: *Up Left*: Two interacting stars which are identified by the N-body code. *Up Right*: These are expanded into their component stars. *Down Right*: Then, are integrated to completion by a standalone small-N code. *Down Left*: Finally, are reinstated into the N-body code. Figure by Zwart and McMillan (2018)

As can be seen in Figure 2.0.2, when two particles approach to each other within the sum of their dynamical radii, the code will stop and the control is passed to multiples so the interaction can be analyzed. The radii are typically chosen to be the 90°tournaround distance $r_{90} \sim GM/ < v^2 >$ in the context of a single star and a few outer binary semimajor axes in a multiple system. When a virial equilibrium in considered and with N-body units, this distance is 1/2N. After the detection of a dynamical interaction and confirming it through some basic tests (such as verifying that the centers of mass are actually approaching), the internal structures of the interacting bodies are restored from the multiples database and the dynamics of the resulting small-N system are then followed until completion by the use of a dedicated code.

Chapter 3

Method

3.1 Ursa Mayor II

Zucker et al. (2006) studied a prominent stellar overdensity around the north galactic pole, in the constellation Ursa Major, by using the imaging and spectroscopic survey SDSS data realease 4, because Grillmair (2006) stated that this overdensity may be a "new globular cluster or dwarf spheroidal".

After analyzing this data, they used Subaru telescope for deeper follow-up observations with the Suprime-Cam mosaic imager. Which allowed to see clearly the shape of the densely populated upper main sequence and sub-giant branch.

However, the width of the upper main sequence far exceeds the observational errors and the expected range in foreground extinction (Zucker et al., 2006). That width could be explained by different factors, one of them is a mix in stellar populations, metallicities and ages. This specific case is ilustrated in the Upper right panel of Figure 3.1.1 where they overplotted three different isochrones with different ages and metallicities from Girardi et al. (2004). The conclusion that they arrived with this is that the object is of intermediate metallicity and with an age of at least 10 Gyrs.

From the isochrones they estimated a distance modulus of 17.5. With that distance, the angular extent of the object becomes $\sim 250 \times 125$ pc. Using the method proposed by Belokurov et al. (2006) the absolute magnitude gave a value of $M_v \sim -3.6$. Finally, because of the size and the extremely low surface brightness

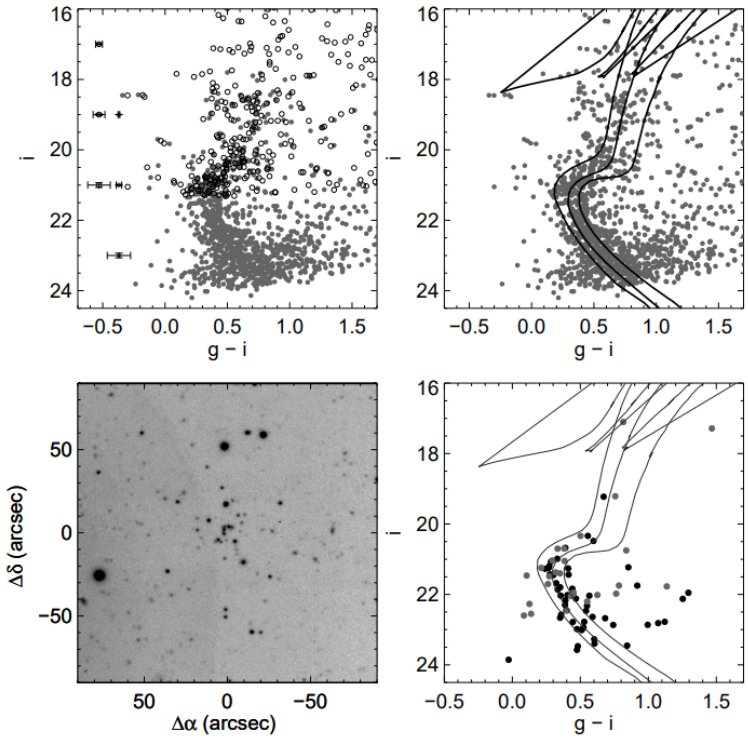

Figure 3.1.1: *Upper left:* Shows a Color Magnitud Diagram (CMD) of the central parts of the object studied, with the black circles from SDSS and the faint dots from Subaru. The detections of the same star but in both photometric data has not been removed. On the left, the error bars indicate the typical photometric error in each data set for $i - band$ magnitud. The width in the error bars of the upper main sequence are by far bigger than observational errors and the expected range in foreground extinction. *Upper right:* Same CMD than before, but this time the grey dots are all the photometric data and the black lines are Padove isochrones (Girardi et al. 2004) with different metalicities and ages. From left to right the overplotting mettalicites and ages are [Fe/H]= -2.3/12 Gyr, [Fe/H]= -1.3/12 Gyr and [Fe/H]= -0.7/10 Gyr; shifted by a distance modulus of 17.5. *Lower left:* G-band image of the apparent central cluster of the object, obtained by Subaru. The image spans 3'x3'. The shadow on the left of the image is the light from a nearby bright star. *Lower right:* Composite CMD of the apparent central cluster of the object (lower left), the black dots are data from SDSS and grey from Subaru. Same isochrones from Upper right panel are overplotted again, but this time the middle isochrone ([Fe/H]= -1.3/12 Gyr) is an apparent good fit of the data. Although, because of the photometric errors, the main sequence is broader than might be expected. Figure by Zucker et al. (2006)

they conclude that the object is a dSph galaxy. As there already is a dSph in said constellation, they named it Ursa Major II (UMa II), the faintest dSph in the MW (at the moment of the discovering). Which has a bright central concentration

Parameter	Value	Reference
RA	08h 51m 30.0s	Zucker et al. (2006)
DEC	+63°07' 48"	
Aparent magnitude (v)	14.3 ± 0.5	
Absolute Magnitude	-3.6	
Distance modulus (μ)	17.5	
Distance	32 ± 4 [kpc]	Wolf et al. (2010)
Luminosity	$4\ ^{+2.5}_{-1.4} \times 10^3 L_\odot, v$	
$r_{1/2}$	140 ± 25 [pc]	
$M_{1/2}$	$7.91\ ^{+5.59}_{-3.14} \times 10^6 M_\odot$	

Table 3.1.1: Summary of the observational parameters of Ursa Major II

and is in the late stages of tidal disruption Simon and Geha (2007). This will be the UFdSph galaxy that we'll be studying and simulating. The important observational measurements are given in Table 3.1.1

3.2 Plummer Potential

For this project, an analytical background density is considered to mimick the DM halo, namely Plummer density distribution

$$\rho(r) = \frac{3M_{Pl}^3}{4\pi R_{Pl}} \left(1 + \frac{r^2}{R_{Pl}^2}\right)^{-\frac{5}{2}}, \tag{3.2.1}$$

where M_{Pl} represents the Plummer mass, which is the total mass of the cluster, R_{Pl} the Plummer radius that represents a scale parameter. Then, the corresponding potential is calculated as

$$\Phi_P(r) = -\frac{GM}{\sqrt{r^2 + R_{Pl}^2}}, \tag{3.2.2}$$

where G is Newton's gravitational constant. The mass enclosed within radius r is given by

$$M(r_{1/2}) = \frac{M_{Pl} r_{1/2}^3}{R_{Pl}^3} \left(1 + \frac{r_{1/2}^2}{R_{Pl}^2}\right)^{-3/2} \tag{3.2.3}$$

In our simulations, the Plummer radii chosen are $R_{Pl} = 50, 100, 250$ and 500

$R_{Pl}[pc]$	$M_{Pl}[M_\odot]$
50	9.4×10^6
100	1.4×10^7
250	6.9×10^7
500	4×10^8

Table 3.2.1: Summary of the M_{Pl} obtained with (3.2.3) and the corresponding R_{Pl} for Ursa Major II

[pc], with the mass enclosed of $M(r_{1/2}) = 7.9 \times 10^6 M_\odot$ and a half light radius of $r_{1/2} = 140$ pc. These parameters are chosen in order to analyze the influence of the DM halo on the final object and if we can reproduce the kinematics properties of Ursa Major II. The observational parameters were taken from Wolf et al. (2010). By the use of the equation (3.2.3), we can obtain the Plummer mass (M_{Pl}) to each R_{Pl}, the Table 3.2.1 summarize the corresponding M_{Pl} .

3.3 Initial Conditions

The central region of the DM halo will be populated with an initial fractal distribution, following the method proposed by Goodwin and Whitworth (2004). Here, a fractal dimension of D =1.6, and a cube size $N_{div} = 2$ were considered, same as in Aravena et al. (2019). The stellar component is formed by 4000 particles with equal mass of $M_* = 0.5$ $M_\odot$, but with a virial ratio of 0, which means that the system is not in virial equilibrium. The total mass of the distribution is calculated by $M_{tot} = N \cdot 0.5$, giving $M_{tot} = 2000$ $M_\odot$. The fractal radius values that were used are $r_{frac} = 50, 100, 200, 400$ and 500 [pc]. These values are listed in Table 3.3.1.

In Figure 3.3.1 the initial fractal distribution for four of the five repetitions performed for a cluster with 4000 stars within a fractal radius of $r_{frac} = 100$ [pc] and a Plummer distribution of $R_{Pl} = 250$ [pc] are shown. The initial stars distribution are completely different in each scenario, because each one have a different random seed, this allows that one repetition is never the same as another.

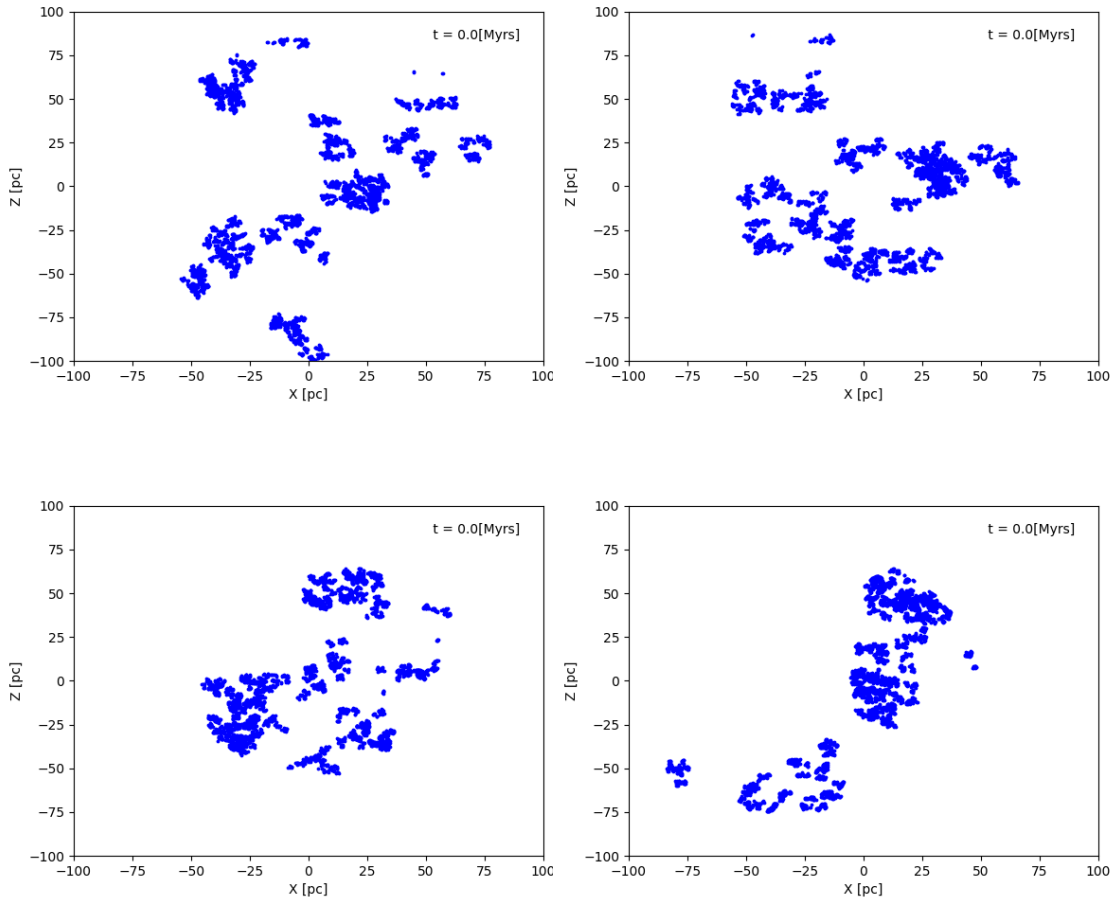

Figure 3.3.1: Examples of initial fractal distribution for four of the five simulations with a fractal size of $r_{frac} = 100$ [pc], Plummer radius and mass of $R_{Pl} = 250$ [pc] and $M_{Pl} = 6.9 \times 10^7 [\mathrm{M}_\odot]$ respectively. As these are not in virial equilibrium, the virial ratio is $\alpha = 0$, so these stellar components spawns with velocities in zero. The four of these have the same parameters, however the random seed for the fractal is what makes them start different.

Parameter		Value
Number of particles	N_*	4000
Mass of the particles	M_*	0.5 $\mathrm{M}_\odot$
Fractal dimension	D	1.6
Cube size	N_{div}	2
Virial ratio	α	0
Total mass of the distribution	M_{tot}	2000 $\mathrm{M}_\odot$
Fractal radius	r_{frac}	[50, 100, 200, 400, 500]

Table 3.3.1: Summary of the initial conditions of the stars in a fractal distribution

Chapter 4

Results

The evolution of the fractal distribution is followed for 1 Gyr . Each parameter set consists of 5 realizations in which the random number seed is the only variable, in order to explore different initial distributions.

4.1 Evolution of the object

The evolution of the object is very similar for all the simulations, even with different parameters they all share one thing, an initial collapse. A good example of this behaviour can be seen in Figure 4.1.1, where we can clearly see that the object collapse towards its center at 15 Myrs. Then, the stars pass through the center and starts a loop between collapsing and expanding. This cycle seems to stabilize near 500 Myrs. However, at 1 Gyr the stars are still oscillating through the center. This is the predicted scenario, because of the nature of a non virial equilibrium system, which indeed collapsed. Although, at first, the final form of the object doesn't seem to reassemble a typical dSph.

This evolution is very different from Cabello Cabello et al. (2023), who simulated UMa II in virial equilibrium. In their scenario, the galaxy did not experience a strong initial collapse and approximately at 500 Myr starts to form a spherical shape.

In order to analyze if 1 Gyr is not enough time for the object to become spherical, we run a simulation with the parameters $R_{Pl} = 500$ pc and $r_{frac} = 500$ pc during 5 Gyr, obtaining the Figure 4.1.2. We can observe that after 1 Gyr the shape of

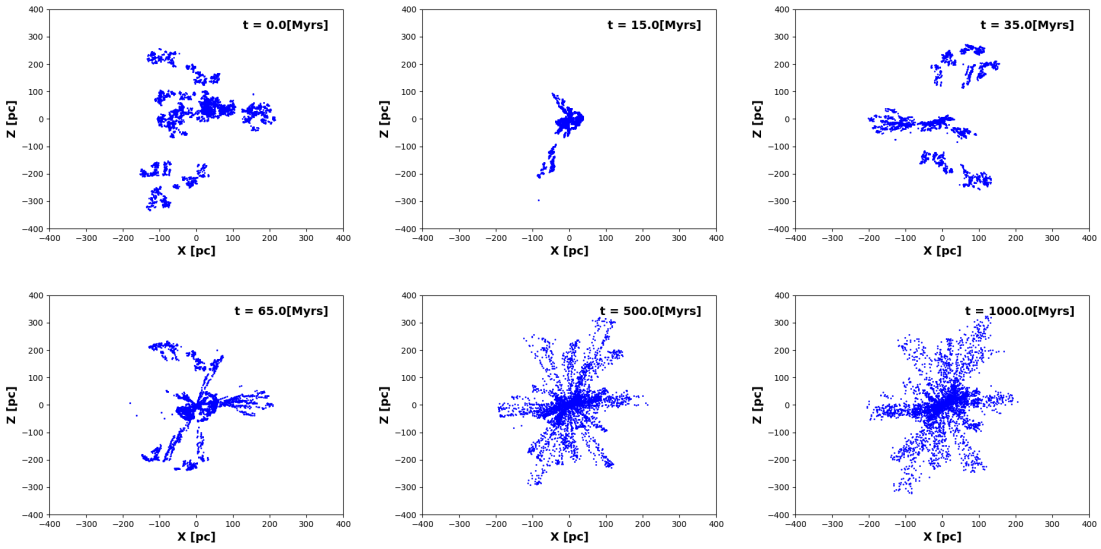

Figure 4.1.1: Example of evolution of fractal distribution with 4000 particles during 1 Gyr for a fractal radius of $r_{frac} = 400$ pc and with an analytical halo of $R_{Pl} = 250$ pc. The six panels represents different stages of the evolution from 0 to 1 Gyr.

the object doesn't really change too much, which leads us to conclude that the final form of our galaxy does not reassemble the spherical shape of a typical dSph. As the initial fractal distribution is different in each repetition, the shape of the object in Figure 4.1.2 and Figure 4.1.1 are different. Although they don't have the same parameters, is safe to assume that the final form of the object depends on the distribution of the initial fractal.

4.2 Size of the final object

4.2.1 Lagrangian Radii

A Lagrangian radii is the radius of an imaginary sphere about the centre of a stellar system containing a fixed proportion of its mass (Sweatman, 1993). In this work, we use the Lagrangian radii at 50% for 1 Gyr of evolution as a function of the Plummer radius.

In Figure 4.2.1 we can observe that not in every scenario the final object evolves into a stable object. On the first two panels, where the fractal radius is 50 and 100 pc from top to bottom, we notice that the first one only stabilize for $R_{Pl} = 50$ pc (blue dots), meanwhile the second one becomes stable for $R_{Pl} = 50$ and 100 pc

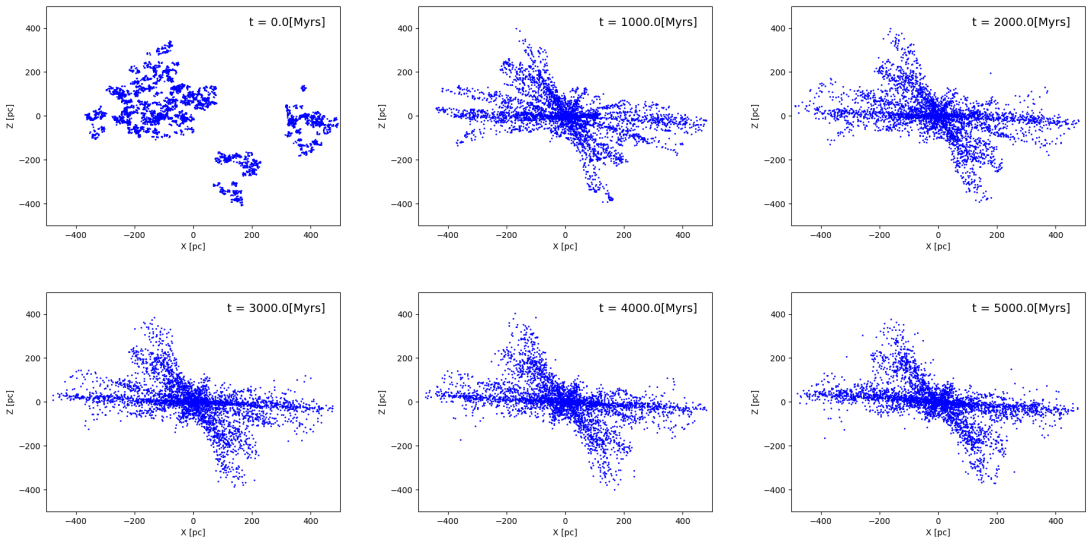

Figure 4.1.2: Evolution of fractal distribution with 4000 particles during 5 Gyr for a fractal radius of $r_{frac} = 500$ pc and with an analytical halo of $R_{Pl} = 500$ pc. The six panels represents the evolution of the object every 1 Gyr.

(blue and orange dots respectively). On the other hand, when the fractal radius is much bigger than the DM halo, the R_{50} will tend to be constant earlier, like in the last panel, where $R_{Pl} = 50$ pc and $r_{frac} = 500$ pc. This happens because, in the first case, we have an homogeneous density sphere (which does not have violent relaxation) collapsing, also here we have almost mass-less particles, so the fractal will collapse into something smaller. The solution here is an harmonic oscillator. In the other case the density gradient of the background turns the velocity into tangential velocity, which helps to calm the ambiance (the bigger fractal). This could be seen if we remove the background potential. We can conclude that if the DM halo is much bigger than the fractal radius, we will not obtain an stable object at least in 1 Gyr. But when the DM halo is smaller than the fractal radius we will obtain an stable object which will slightly oscillate.

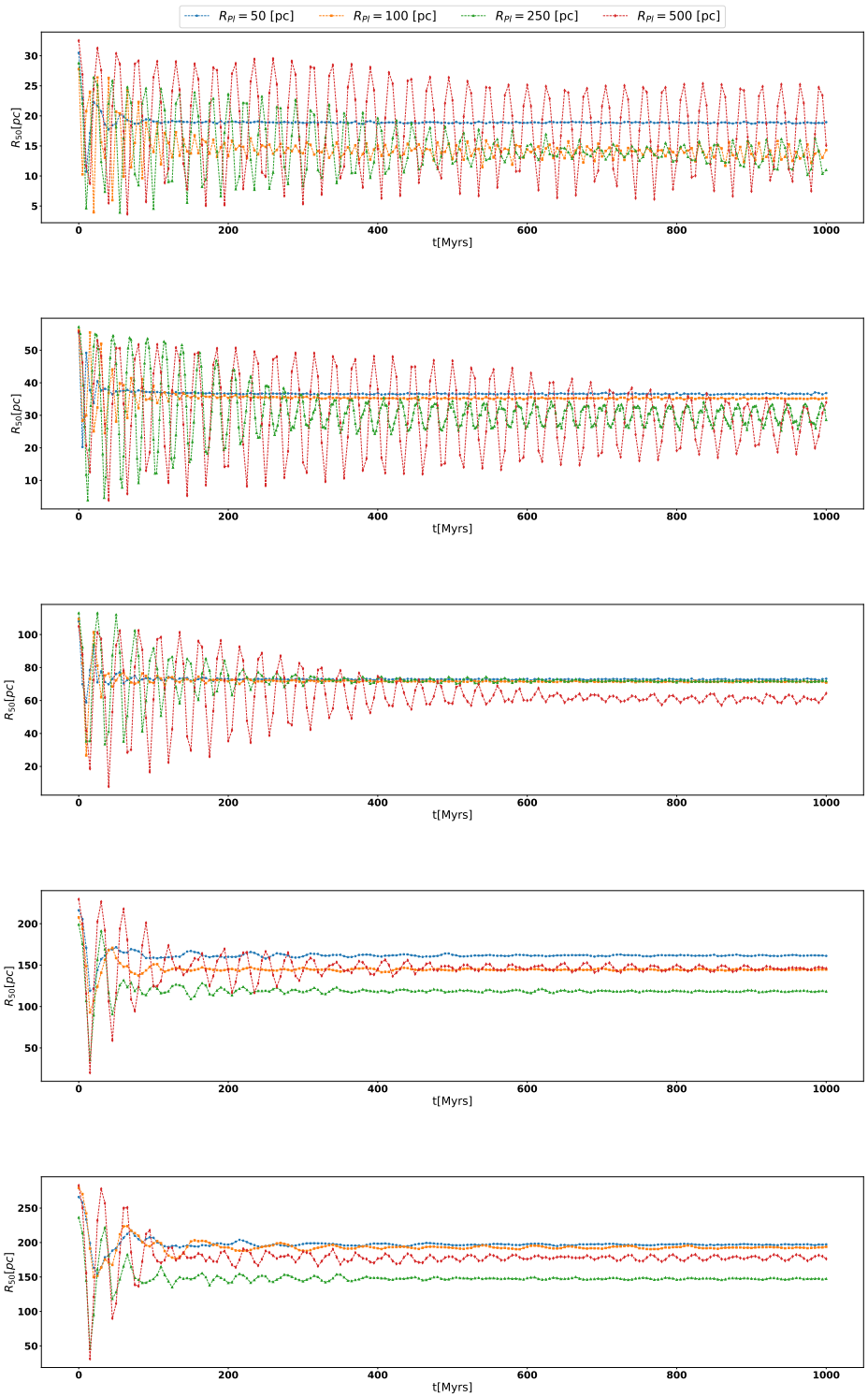

Figure 4.2.1: Lagrangian radii at 50% [pc] plotted vs time of evolution of the simulation (1Gyr). The first panel considers a fractal radius of 50 [pc], the second a fractal radius of 100[pc], the third a fractal radius of 200[pc], the fourth a fractal radius of 400, and the last panel a fractal radius of 500[pc]. The colored dots from blue, orange, green and red; represents the Plummer radius of 50, 100, 250 and 500 [pc] respectively. Error bars are omitted.

For UMa II, in a virial equilibrium scenario, this doesn't happen, because in the same amount of time, the Lagragian radius becomes almost constant independent of the value of the Fractal or Plummer radius (Cabello Cabello et al., 2023), the same with simulations of others dSph in virial equilibrium such as Segue 1 (Aravena et al., 2019). In both scenarios, if they increase the initial Plummer Radius the object needs more time to stabilize independent of the fractal distribution initially selected. Here we can observe the same tendency in Figure 4.2.1, as at $R_{Pl} = 500$ pc (red dots) are always the last objects to become stable. However, how fast it becomes stable does depend on the fractal radius, because at larger r_{frac} it stabilizes earlier as can be seen comparing $R_{Pl} = 500$ on last two panels, where in the last one ($r_{frac} = 500$ pc) the object needed ~ 170 Myr to become stable, meanwhile on the other panel ($r_{frac} = 400$ pc) the object needed ~ 300 Myr.

We considered the R_{50} at 1 Gyr, which in almost every simulation match with the mean half mass radius considering the whole evolution, due to at 1 Gyr the majority of simulations have already stabilized. In the cases where 1 Gyr is not enough to become stable, we calculated the mean half mass radius considering each R_{50} every 200 Myrs during 1 Gyr. The mean values of the R_{50} from each simulation are listed in Table 4.2.1, by using this data we obtain Figures 4.2.1 and 4.2.2.

Figure 4.2.2 on the top panel, shows the half mass radius against the Plummer radius for each initial fractal distribution, while the bottom panel shows the half mass radius against the fractal radius for each Plummer distribution. From both panels we can conclude that the dependency of the half mass radius is almost entirely on the fractal radius, being directly dependent, because at bigger fractal radii, bigger R_{50} values; also bigger error bars. Yet, the dependency on the Plummer radius is almost non existent with the R_{50}, with few exceptions like $R_{Pl} = 500$ pc at $r_{frac} = 250$ pc, which is the only Plummer radius for that fractal radius where the half mass radius is very close to the observational.

We can observe that at initial fractal distributions lower than 350 pc the results fail to reproduce the observational data, turning into objects way smaller than intended. While a fractal radius higher than 450 pc seems to be closer. In conclusion, we need fractal distributions between 350-450 pc to reproduce the half mass radius of UMa II, from our simulations, a fractal radius of 400 pc is the closest to the observed.

R_{Pl} [pc]	r_{frac} [pc]	R_{50} [pc]
50	50	18.964 ± 1.27
	100	36.756 ± 5.277
	200	73.076 ± 15.992
	400	161.858± 14.640
	500	197.511± 40.784
100	50	14.495±3.731
	100	35.518±4.584
	200	71.936±13.015
	400	145.003±21.778
	500	193.702±39.961
250	50	14.724±3.727
	100	31.014±7.182
	200	72.512±8.348
	400	119.678±25.507
	500	148.654±15.432
500	50	18.538±4.580
	100	30.263±5.036
	200	63.498±22.302
	400	147.176±45.96
	500	178.857±51.687

Table 4.2.1: Mean R_{50} values obtained of the corresponding R_{Pl} and r_{frac}.

Aravena et al. (2019) showed that the R_{50} value depends mainly on the DM halo size, same happens with Cabello Cabello et al. (2023), where they showed that for UMa II in a virial quilibrium scenario the half mass radius for UMa II needs a DM scale-lenght of 200-250 pc. This result gives us two different ranges of values with different dependencies, which means that the initial virial condition of the object will determine if the size of object will depend on the DM halo or the fractal distribution.

4.2.2 Final and initial R_{50}

In order to verify the previous results. We compare the initial R_{50} vs the final R_{50} of each simulation, to see how much the size of the final object depends on fractal or Plummer radius.

In Figure 4.2.3 we see the same result as before, that the final object does not depend on the size of the DM halo (*Right* panel), but also that it only depends on the size of the initial fractal distribution (*Left* panel). Another thing to notice

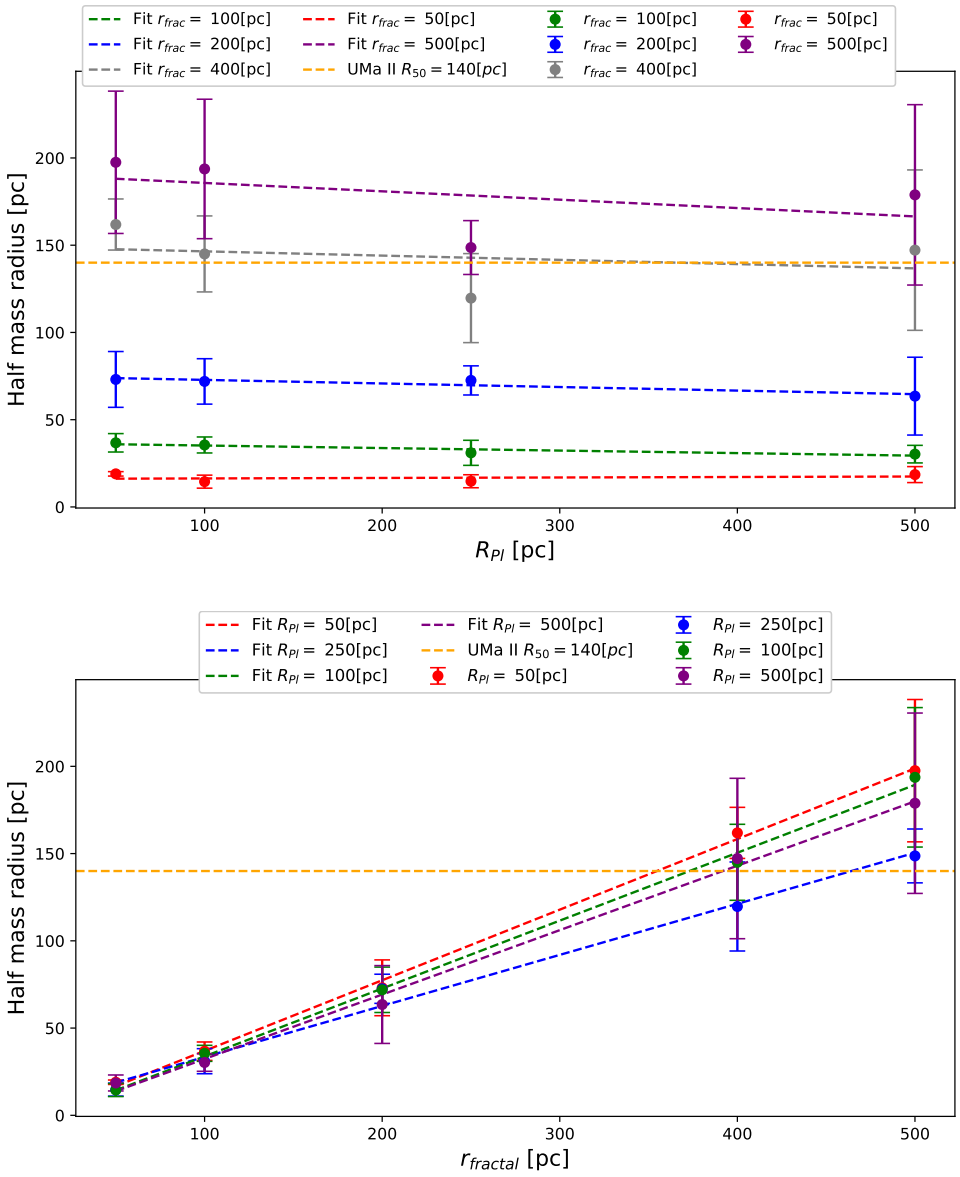

Figure 4.2.2: Comparisson between R_{50} and the dependency of Plummer and fractal radius, and how close are these values to Ursa Major II real R_{50}. *Upper Panel:* R_{50} vs R_{Pl}, the colors purple, grey, blue, green and red; represents $r_{frac} = 500, 400, 200, 100$ and 50 [pc] respectively, the dotted lines are the fit for each color. *Bottom Panel:* R_{50} vs r_{frac}, the colors purple, blue, green and red; represents $R_{Pl} = 500, 250, 100$ and 50 [pc] respectively, the dotted lines are the fit for each color.

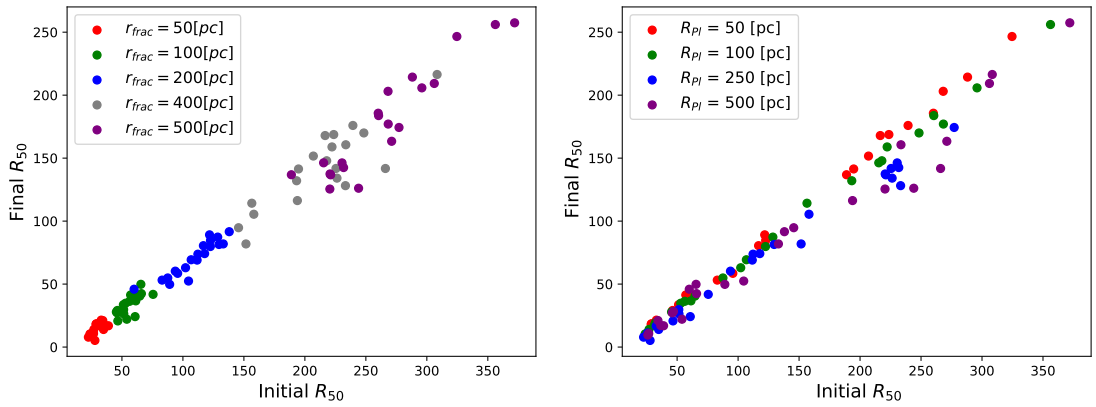

Figure 4.2.3: Comparisson between initial and final R_{50}, both axis are in parsec. *Left:* Colored dots: red, green, blue, grey and purple; represent the values of $r_{frac} = 50, 100, 200, 400$ and $500[pc]$; respectively. *Right:* Colored dots: red, green, blue, purple; represent $R_{Pl} = 50, 100, 250$ and 500; respectively.

is the initial R_{50} is always bigger than the final value, we can conclude that the final object depends on the initial half mass radius. Also, for bigger initial fractal there is a bigger range for the final R_{50}, which will lead to larger error bars.

The size of the DM is not relevant in the size of the half mass radius. As a result, measuring the half mass radius of a UFdSph is not enough to calculate the DM distribution in a collapsing scenario.

4.3 Velocity dispersion

The velocity dispersion allows to determine the standard deviation for the mean velocity of the particles within the system. For the calculation of the velocity dispersion σ we considered all the stars within the half mass radius that spans across two coordinates, i.e we obtained the Line-of-sight (LOS) in each coordinate. The mean values with their respective errors are recompiled in Table 4.3.1.

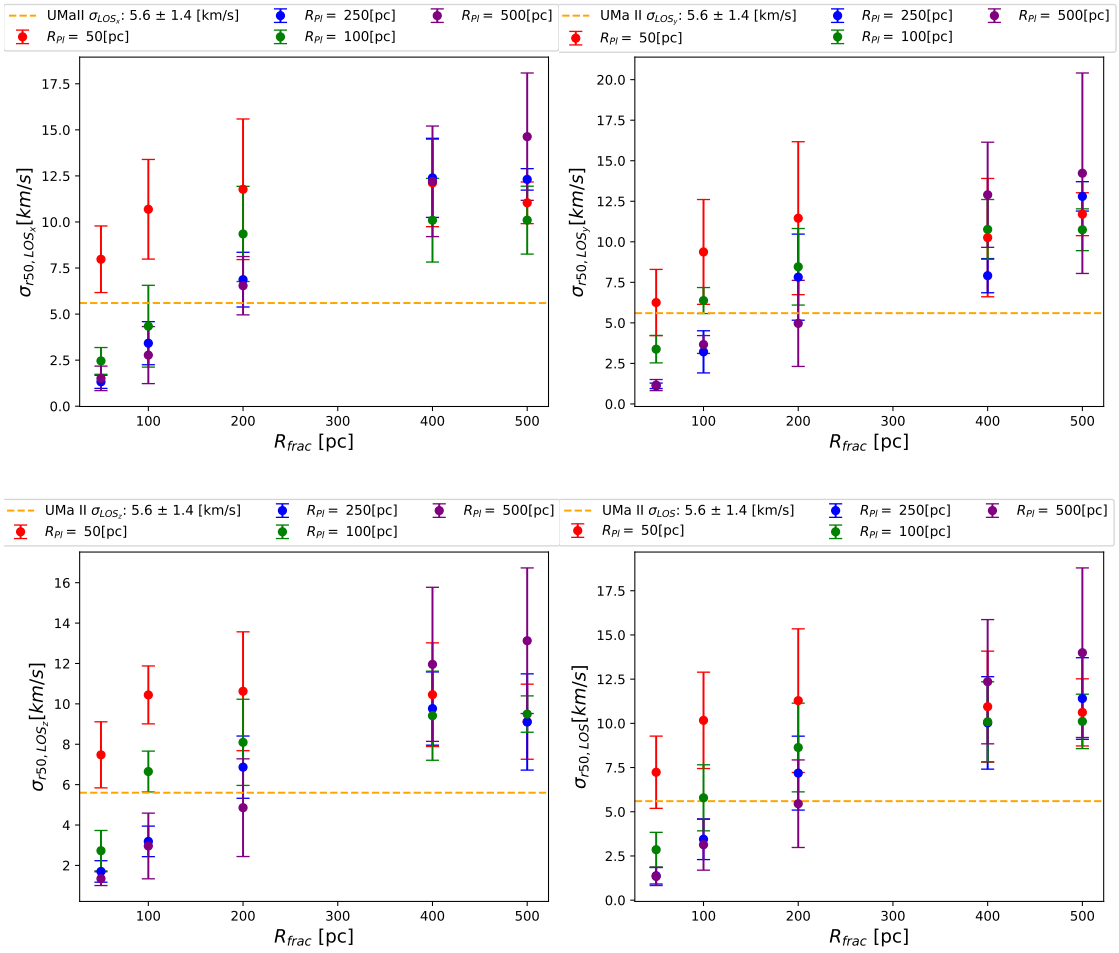

Figure 4.3.1: Line of sight of velocity dispersion of the simulations vs the fractal radius. The colored dots represent different DM halo scale lenghts. The yellow line is the actual velocity dispersion of UMa II. *Upper Left:* This panel shows the velocity dispersion for σ_{r50,LOS_x}. *Upper Right:* This panel shows the velocity dispersion for σ_{r50,LOS_y}. *Down Left:* This panel shows the velocity dispersion for σ_{r50,LOS_z}. *Down Right:* This panel shows the mean velocity dispersion considering the previous three graphs, and all the data from Table 4.3.1.

R_{Pl} [pc]	r_{frac} [pc]	σ_{r50,LOS_x}	σ_{r50,LOS_y}	σ_{r50,LOS_z}
50	50	7.976±1.807	6.254±2.043	7.476±1.636
	100	10.689±2.704	9.375±3.232	10.443±1.434
	200	11.774±3.816	11.455±4.717	10.624±2.943
	400	12.117±2.372	10.258±3.649	10.455±2.567
	500	11.04±1.131	11.702±1.323	9.117±1.859
100	50	2.458±0.726	3.379±0.847	2.729 ± 1
	100	4.342±2.22	6.377±0.802	6.649 ±1.011
	200	9.35±2.583	8.458±2.36	8.095 ±2.134
	400	10.094±2.27	10.764±1.844	9.413 ±2.206
	500	10.098±1.842	10.743±1.289	9.495±0.9
250	50	1.323±0.357	1.118 ±0.168	1.701 ±0.532
	100	3.419±1.169	3.213 ±1.3	3.19±0.756
	200	6.869±1.485	7.819±2.655	6.866±1.541
	400	12.394±2.147	7.911±1.054	9.768±1.813
	500	12.311±0.583	12.801±0.906	9.103±2.383
500	50	1.511±0.665	1.164±0.342	1.344±0.341
	100	2.773±1.547	3.666±0.551	2.963±1.626
	200	6.54±1.582	4.968±2.655	4.859±2.419
	400	12.206±3.001	12.9±3.242	11.958±3.815
	500	14.63±3.456	14.229±6.182	13.127±3.605

Table 4.3.1: Line of sight of velocity dispersion from each simulation in (y,z), (x,z) and (x,y)

Now we can compare the velocity dispersion obtained with the value observed for UMa II. (Simon, 2019) determine the observational LOS of UMa II $\sigma_{LOS} = 5.6\pm1.4$ km s^{-1}.

In Figure 4.3.1 we show the three directions of the LOS and the mean between them as a function of fractal radius for each Plummer distribution. It is expected that in a spherical object, the three plots would have the same values, and they are quite similar, but with big error bars. Focusing on the bottom right panel, which is the mean, we can observe that at fractal radii between [50 - 200] pc the obtained values of velocity dispersion are very close to the observed in UMa II, but depending on the Plummer radius they are closer or further. This is the first time that we observe a dependency on the DM halo distribution. In the same range, we can also observe a strong dependency of the velocity dispersion, which increase with the fractal radius. However, between a fractal radius of $[400 - 500]$ pc the values becomes almost constant. This change on the tendency could be due $\sigma \propto M/r$, in the case of $R_{Pl} = 100$ pc (green dots) we have all the mass contained

in 100 pc (fractal radius). Thus, when we observe this model at $r_{frac} = 200$ pc we have the doble radius, but the same mass. This might explain why the only model that keeps increasing is when the $R_{Pl} = 500[pc]$.

In previous subsections we determined that the initial fractal distribution that gives us the half mass radius closest to the observational is between [350-450] pc. Nevertheless, the velocity dispersion between that range is way bigger than expected. Cabello Cabello et al. (2023) also have the same situation, but none of their values were close to the observed. Thus, neither them nor our results in simulations could replicate the observed velocity dispersion on UMa II using the observed half mass radius. However, we could expect that, if our model is correct, we would obtain an overestimation of the DM mass, because on the observations a lot of assumptions such as a spherical, isotropic and with no rotation model are used. We would need lower DM mass, as deduced from observations, to replicate those velocity dispersion.

Chapter 5

Conclusions

We studied a theorical model for a possible formation scenario for dSph galaxies, originally proposed by Assmann et al. (2013) and adapted for UFdSph galaxies by Aravena et al. (2019). We simulated Ursa Major II using AMUSE and the direct N-body integrator ph4. Considering 4000 particles in a fractal distribution within a DM halo with a range of different sizes, in non virial equilibrum, following the evolution over 1 Gyr. Every combination of parameters consists of 5 realizations, amounting to a total of 110 simulations. From our results we can conclude the following:

Through the evolution of the galaxy we can observe that even with different parameters and initial fractal distribution, all of our simulations presents a strong collapse initially, that even after 5 Gyr does not reassemble the spherical shape of a typical dSph. The shape of the final object relies completely on the distribution of the initial fractal

Analyzing the Lagrangian radii at 50% of the mass we can observe that depending on the parameters the object will evolve into a stable object or not. When the DM halo scale-length is smaller than the fractal radius, the R_{50} will tend to become stable, at larger fractal radii the process will be faster. On the other hand, when the DM halo scale-length is much larger than the fractal radius the, R_{50} will not become constant during 1 Gyr, and at even larger Plummer radii the object will need even more time and maybe keep on oscillating until today.

The final size of the object depends on the initial half mass radius which is determined completely by the fractal radius. These results are contrary to the

virial equilibrium scenario (Cabello Cabello et al., 2023). To reproduce the half mass radius of UMa II we would need a fractal radius between 350-450 pc. The size of the DM halo does not play a relevant role on the R_{50} in the collapsing scenario, which means that we would not be able to deduce scale-length of the DM distribution of a UFdSph galaxy by measuring their half mass radii. Finally, we can conclude that the initial virial condition of the object will determine whether the size dependence lies with the DM halo or the fractal distribution.

The velocity dispersion has a direct dependency with the fractal radii. However, we also observe a dependency on the Plummer Radius, with which, at fractal radii between 50-200 pc, we obtain values closer or further to UMa II. Nevertheless, at the range previously determined to reproduce the half mass radius of UMa II we get velocity dispersions much higher than the observed. As the observational models consider an ideal scenario, we would need to lower DM halo mass to match those results.

In the future we expect to analyze these results with the Navarro-Frenk-White (NFW) model of UMa II in virial equilibrium so we can have an extended analysis of the formation model and how the different scenarios affects the dependency on the parameters and the evolution of the object.

Bibliography

Alarcón Jara, A. G., Fellhauer, M., Simon, J., del Pino, A., Fu, S. W., and Sohn, S. T. (2023). Detection of chemo-kinematical structures in leo i. *Astronomy Astrophysics*, 672.

Aravena, C., Fellhauer, M., Zapata, F. U., and Jara, A. A. (2019). A formation scenario for faint and ultra-faint dwarf spheroidal galaxies. *Boletín de la Asociación Argentina de Astronomía*, 61a:181–183.

Assmann, P., Fellhauer, M., Wilkinson, M. I., and Smith, R. (2013). A possible formation scenario for dwarf spheroidal galaxies – i: Fiducial model. *Monthly Notices of the Royal Astronomical Society*, page 1–12.

Belokurov, V., Zucker, D. B., Evans, N. W., Gilmore, G., Vidrih, S., Bramich, D. M., Newberg, H. J., Wyse, R. F. G., Irwin, M. J., Fellhauer, M., Hewett, P. C., Walton, N. A., Wilkinson, M. I., Cole, N., Yanny, B., Rockosi, C. M., Beers, T. C., Bell, E. F., Brinkmann, J., Ivezić, , and Lupton, R. (2006). The field of streams: Sagittarius and its siblings. *The Astrophysical Journal*, 642:L137–L140.

Bland-Hawthorn, J., Karlsson, T., Sharma1, S., Krumholz, M., and Silk, J. (2010). The chemical signatures of the first star clusters in the universe. *The Astrophysical Journal*, 721.

Bosma, A. (1978). Phd thesis: The distribution and kinematics of neutral hydrogen in spiral galaxies of various morphological types. *University of Groningen.*

Bovill, M. S. and Ricotti, M. (2011). Where are the fossils of the first galaxies? i. local volume maps and properties of the undetected dwarfs. *The Astrophysical Journal*, 741.

Bullock, J. S. and Boylan-Kolchin, M. (2017). Small-scale challenges to the λcdm paradigm. *Annual Review of Astronomy and Astrophysics*, 55:343–387.

Cabello Cabello, J., Fellhauer, M., and Mtaus-Carrillo, D. (2023). The formation of faint and ultra-faint dwarf spheroidal galaxies: Modeling the formation of ursa major ii using amuse. *poster at LARIM.*

de Blok, W. (2010). The core-cusp problem. *Advances in Astronomy*, 2010.

de Blok, W. J. G., Bosma, A., and McGaugh, S. (2003). Simulating observations

of dark matter dominated galaxies: towards the optimal halo profile. *Monthly Notices of the Royal Astronomical Society*, 340.

D'Onghia, E., Besla, G., Cox, T. J., and Hernquist, L. (2009). Resonant stripping as the origin of dwarf spheroidal galaxies. *Nature*, 460:605–607.

Fellhauer, M., Kroupa, P., Baumgardt, H., Bien, R., Boily, C., Spurzem, R., and Wassmer, N. (2000). Superbox – an efficient code for collisionless galactic dynamics. *New Astronomy*.

FUJII, M., IWASAWA, M., FUNATO, Y., and MAKINO, J. (2007). Bridge: A direct-tree hybrid n -body algorithm for fully self-consistent simulations of star clusters and their parent galaxies. *Astronomical Society of Japan*, 59(6):1095–1106.

Fujii, M., Iwasawa, M., Funato, Y., and Makino, J. (2008). Evolution of star clusters near the galactic center: Fully self-consistent n-body simulations. *The Astrophysical Journal*, 686(2):1082–1093.

Girardi, L., Grebel, E. K., Odenkirchen, M., and Chiosi, C. (2004). Theoretical isochrones in several photometric systems ii. *Astronomy & Astrophysics*, 422:205–215.

Goodwin, S. P. and Whitworth, A. P. (2004). The dynamical evolution of fractal star clusters: The survival of substructure. *Astronomy and Astrophysics*, 413:929–937.

Grillmair, C. J. (2006). Substructure in tidal streams: Tributaries in the anticenter stream. *The Astrophysical Journal*, 651:L29–L32.

Kirby, E. N., Cohen, J. G., Guhathakurta, P., Cheng, L., Bullock, J. S., and Gallazzi, A. (2013). The universal stellar mass-stellar metallicity relation for dwarf galaxies. *The Astrophysical Journal*, 779.

Kormendy, J. and Freeman, K. C. (2004). Scaling laws for dark matter halos in late-type and dwarf spheroidal galaxies. *International Astronomical Union Symposium*, 220.

Makino, J. and Aarseth, S. J. (1992). On a hermite integrator with ahmad-cohen scheme for gravitational many-body problems. *Publications of the Astronomical Society of Japan*, 44:141–151.

Martin, N. F., Ibata, R. A., Chapman, S. C., Irwin, M., and Lewis, G. F. (2007). A keck/deimos spectroscopic survey of faint galactic satellites: searching for the least massive dwarf galaxies. *Monthly Notices of the Royal Astronomical Society*, 380.

Mayer, L., Kazantzidis, S., Mastropietro, C., and Wadsley, J. (2007). Early gas stripping as the origin of the darkest galaxies in the universe. *Nature*, 445:738–740.

Munoz, R. R., Carlin, J. L., Frinchaboy, P. M., Nidever, D. L., Majewski, S. R., and Patterson, R. J. (2006). Exploring halo substructure with giant stars: The dynamics and metallicity of the dwarf spheroidal in bootes. *The Astrophysical Journal*, 650.

Navarro, J. F., Frenk, C. S., and White, S. D. M. (1996). The structure of cold dark matter halos. *Astrophysical Journal*, 462.

Pelupessy, F., van Elteren, A., de Vries, N., McMillan, S., Drost, N., and Zwart, S. P. (2013). The astrophysical multipurpose software environment. *Astronomy & Astrophysics*.

Peñarrubia, J., Navarro, J. F., and McConnachie, A. W. (2008). Local group dwarf galaxies in the λcdm paradigm. *Astronomische Nachrichten*, 329.

Rubin, V. C., Ford, W. K., Jr., and Thonnard, N. (1978). Extended rotation curves of high-luminosity spiral galaxies. iv. systematic dynamical properties, $sa \rightarrow sc$. *The Astrophysical Journal*, 225:L107–L111.

Sawala, T., Scannapieco, C., Maio, U., and White, S. D. (2009). Formation of isolated dwarf galaxies with feedback. *Monthly Notices of the Royal Astronomical Society*, page 1–17.

Shapley, H. (1938). A stellar system of a new type. *Harvard College Observatory Bulletin*, 908:1–11.

Simon, J. D. (2019). The faintest dwarf galaxies. *Annual Review of Astronomy and Astrophysics*.

Simon, J. D. and Geha, M. (2007). The kinematics of the ultra-faint milky way satellites: Solving the missing satellite problem. *The Astrophysical Journal*, 670:313–331.

Sweatman, W. L. (1993). A study of lagrangian radii oscillations and core-wandering using tv-body simulations. *Monthly Notices of the Royal Astronomical Society*, pages 497–512.

Wolf, J., Martinez, G. D., Bullock, J. S., Kaplinghat, M., Geha, M., Muñoz, R. R., Simon, J. D., and Avedo, F. F. (2010). Accurate masses for dispersion-supported galaxies. *Monthly Notices of the Royal Astronomical Society*, 406:1220–1237.

Zucker, D. B., Belokurov, V., Evans, N. W., Kleyna, J. T., Irwin, M. J., Wilkinson, M. I., Fellhauer, M., Bramich, D. M., Gilmore, G., and Newberg, H. J. (2006). A curious milky way satellite in ursa major. *The Astrophysical Journal*, 650:L41–L44.

Zwart, S. P. and McMillan, S. (2018). *Astrophysical Recipes The art of AMUSE*. IOP Publishing.

Łokas, E. L., Kazantzidis, S., and Mayer, L. (2012). How to make an ultra-faint dwarf spheroidal galaxy: Tidal stirring of disky dwarfs with shallow dark matter density profiles. *The Astrophysical Journal Letters*, 751:L15.

Appendix A

Code

```
1     #!/usr/bin/env python
2
3  from amuse.units import units, nbody_system, constants
4  from amuse.datamodel import Particles
5  from amuse.ic.fractalcluster import new_fractal_cluster_model
6  from amuse.community.ph4.interface import ph4
7  from amuse.ext import galactic_potentials
8  from amuse.couple import bridge
9
10 from amuse.community.smalln.interface import SmallN
11 from amuse.community.kepler.interface import Kepler
12 from amuse.couple import multiples
13
14 import numpy as np
15 from sys import exit
16 from os.path import isfile
17 import argparse
18
19 # Este bloque de codigo viene del libro de amuse, para la
   ↪  evaluacion de encuentros cercanos
20 ###BOOKLISTSTART1###
21 SMALLN = None
22 def init_smalln(converter):
```

```
23      global SMALLN
24      SMALLN = SmallN(convert_nbody=converter)
25  def new_smalln():
26      global SMALLN
27      SMALLN.reset()
28      return SMALLN
29  ###BOOKLISTSTOP1###
30
31  def get_opts():
32      par = argparse.ArgumentParser()
33
34      par.add_argument( "--NFW",    help="Use NFW potential",
        ↪  action='store_true', default=False)
35      par.add_argument( "--Plum",   help="Use Plummer potential",
        ↪  action='store_true', default=False)
36      par.add_argument( "--file", help="Use [file] as initial
        ↪  condition", default=None)
37      par.add_argument( "--virial", type=float, help="Set virial
        ↪  ratio", default=0.5)
38      par.add_argument( "-M",   type=float, help="Masa del halo
        ↪  [Msun]", default = 1e4)
39      par.add_argument( "-R",   type=float, help="Radio de escala
        ↪  [pc]", default = 50)
40      par.add_argument( "-Rin", type=float, help="Radio que encierra
        ↪  a M (solo para NFW) [pc]", default = 50)
41      par.add_argument( "-t",   type=float, help="Tiempo simulacion
        ↪  [Myr]", default = 50)
42
43      return par.parse_args()
44
45  def Save_snap(i,t, stars, fo):
46      N = len(stars)
47      header = "{:5.2f} ".format(t.value_in(units.Myr))
48      header += "{:d} ".format(N)
49      header += "{:d}\n".format(N)
```

```
50      fo.write(header)
51
52      for star in stars:
53
54          linea  = "{:5.2f} ".format(star.mass.value_in(units.MSun))
55          linea += "{:5.1f} ".format(star.radius.value_in(units.au))
56          linea += "{:5.6f} ".format(star.x.value_in(units.kpc))
57          linea += "{:5.6f} ".format(star.y.value_in(units.kpc))
58          linea += "{:5.6f} ".format(star.z.value_in(units.kpc))
59          linea += "{:5.6f} ".format(star.vx.value_in(units.kms))
60          linea += "{:5.6f} ".format(star.vy.value_in(units.kms))
61          linea += "{:5.6f}\n".format(star.vz.value_in(units.kms))
62
63          fo.write(linea)
64      fo.write("\n")
65
66  def Save_snap2(i,t, stars):
67      N = len(stars)
68      nombre = "salida_{:05d}.dat".format(i)
69      fo = open(nombre, "w")
70      header = "{:5.2f} ".format(t.value_in(units.Myr))
71      header += "{:d} ".format(N)
72      header += "{:d}\n".format(N)
73      fo.write(header)
74
75      for star in stars:
76
77          linea  = "{:5.2f} ".format(star.mass.value_in(units.MSun))
78          linea += "{:5.1f} ".format(star.radius.value_in(units.au))
79          linea += "{:5.6f} ".format(star.x.value_in(units.parsec))
80          linea += "{:5.6f} ".format(star.y.value_in(units.parsec))
81          linea += "{:5.6f} ".format(star.z.value_in(units.parsec))
82          linea += "{:5.6f} ".format(star.vx.value_in(units.kms))
83          linea += "{:5.6f} ".format(star.vy.value_in(units.kms))
84          linea += "{:5.6f}\n".format(star.vz.value_in(units.kms))
```

```
85
86          fo.write(linea)
87      fo.close()
88
89  def get_from_file(infile, tmax, dt):
90
91      header = open(infile, 'r')
92      linea = header.readline().split()
93      ti = float(linea[0])
94      N = int(linea[1])
95      header.close()
96
97      timesteps = np.arange(0, tmax-ti, dt) | units.Myr
98      ti = ti | units.Myr
99
100     mass, radius, x, y, z, vx, vy, vz = np.genfromtxt(infile,
        ↪  unpack=True, skip_header=1)
101
102     stars = new_fractal_cluster_model(N, converter, random_seed =
        ↪  -77, fractal_dimension=1.6)
103
104     print(len(x))
105
106     stars.mass = mass | units.MSun
107     stars.radius = radius | units.au
108     stars.x = x | units.parsec
109     stars.y = y | units.parsec
110     stars.z = z | units.parsec
111     stars.vx = vx | units.kms
112     stars.vy = vy | units.kms
113     stars.vz = vz | units.kms
114
115     step = int(infile.split("_")[1].split('.')[0])
116
117     return stars, timesteps, ti, step
```

```
118
119
120 # Parametros simulacion
121
122 opt = get_opts()
123 nsteps    = 500                  # Numero de timesteps
124 N         = 4000                 # Numero de particulas
125 t_end     = opt.t | units.Myr    # Tiempo al final de la
    ↪  simulacion
126 dt_snap   = t_end/nsteps         # dt entre cada snapshot
127 dt_bridge = dt_snap/(nsteps)  # dt para el metodo bridge
128 Rfrac     = 100.0| units.parsec # Radio fractal
129 Mcl       = N*0.5 | units.MSun   # Masa total del cumulo
130 Q_virial  = opt.virial
131 ti        = 0.0 | units.Myr
132
133 if opt.NFW:
134     print("Creando NFW halo")
135     rs = float(opt.R)   | units.parsec
136     r  = float(opt.Rin) | units.parsec
137     M  = float(opt.M)   | units.MSun
138     A_nfw = np.log((r+rs)/rs) - r/(r+rs)
139     rho_0 = M/(4*np.pi * rs**3 * A_nfw)
140     halo = galactic_potentials.NFW_profile(rho_0, rs)
141
142 elif opt.Plum:
143     print("Creando Plummer halo")
144     Rpl = float(opt.R) | units.parsec
145     Mpl = float(opt.M) | units.MSun
146     halo = galactic_potentials.Plummer_profile(Mpl, Rpl)
147
148 else:
149     print("No se selecciono un potencial.")
150     print("Cerrando script")
151     exit()
```

```
152
153 #Se crea el fractal
154 converter = nbody_system.nbody_to_si(Rfrac, Mcl)
155 if opt.file is None:
156     stars = new_fractal_cluster_model(N, converter, random_seed =
        ↪ -77, fractal_dimension=1.6)
157     timesteps = np.arange(0, opt.t, dt_snap.value_in(units.Myr)) |
        ↪ units.Myr
158     #stars = new_fractal_cluster_model(N, converter)
159
160     #Se ajustan las posiciones de manera que la distancia maxima
        ↪ al centro del sistema sea igual a rfrac
161     escala_radio = Rfrac / stars.total_radius()
162     stars.position *= escala_radio
163
164     # Asignamos la distancia de interaccion entre estrellas:
165     stars.radius = 1000 | units.au
166     stars.id = np.arange(N)+1
167     i = 0
168 else:
169     stars, timesteps,ti, i = get_from_file(opt.file, opt.t,
        ↪ dt_snap.value_in(units.Myr))
170
171
172 # Se inicializa el codigo Nbody
173 grav = ph4(converter, mode='gpu')
174 grav.initialize_code()
175 grav.particles.add_particles( stars )
176 grav.commit_particles()
177
178 # Cuando 2 particulas pasen muy cerca entre ellas, el codigo debe
    ↪ detenerse y
179 # evaluar el encuentro con Kepler. Esto se logra con un
    ↪ stopping_condition
180 stopping_condition = grav.stopping_conditions.collision_detection
```

```
181 stopping_condition.enable()
182
183 init_smalln(converter)
184 kep = Kepler(unit_converter=converter)
185 kep.initialize_code()
186 multiples_code = multiples.Multiples(grav, new_smalln, kep,
    ↪  constants.G, verbose=False)
187 multiples_code.global_debug = 0
188
189 channel_from_grav_to_stars = grav.particles.new_channel_to( stars
    ↪  )
190 channel_from_stars_to_grav = stars.new_channel_to( grav.particles
    ↪  )
191
192 # Las particulas interactuan con el background potential mediante
    ↪  el metodo "bridge":
193 integrator = bridge.Bridge(verbose=False)
194 integrator.add_system(multiples_code, (halo,))
195 integrator.timestep = dt_bridge
196
197 if opt.file is None:
198     Q_actual = integrator.kinetic_energy /
        ↪  np.abs(integrator.potential_energy)
199
200     print("Q_actual = ", Q_actual)
201
202     if Q_virial>-1:
203         factor = np.sqrt(Q_virial/Q_actual)
204         integrator.particles.velocity *= factor
205         Q_final = integrator.kinetic_energy /
            ↪  np.abs(integrator.potential_energy)
206         print("factor  = ", factor)
207         print("Q_final = ", Q_final)
208
```

```
209 # Para poder imprimir el primer step de forma correcta,
    ↪ recuperamos los valores
210 # desde el integrador
211 channel_from_grav_to_stars.copy_attributes(['x','y', 'z',
    ↪ 'vx','vy', 'vz'])
212
213
214 f = open('archivo.dat', 'w')
215
216 t = 0 | units.yr
217
218
219 Save_snap2(i, 0|units.yr, stars)
220
221
222 # while t < t_end:
223 for t in timesteps:
224     kinetic_energy = integrator.kinetic_energy
225     potential_energy = integrator.potential_energy
226     integrator.evolve_model(t)
227     integrator.synchronize_model()
228     t = integrator.model_time + ti
229
230     channel_from_grav_to_stars.copy_attributes(['x','y', 'z',
        ↪ 'vx','vy', 'vz'])
231     Q_actual = integrator.kinetic_energy /
        ↪ np.abs(integrator.potential_energy)
232     f.write("{},{},{},{}\n".format(t.value_in(units.Myr),
        ↪ kinetic_energy.value_in(units.MSun*units.kms**2),
        ↪ potential_energy.value_in(units.MSun*units.kms**2),
        ↪ Q_actual))
233     print("t = {:2.2f} /
        ↪ {:2.2f}".format(t.value_in(units.Myr),t_end.value_in(units.Myr)))
234
235     # Save_snap(i, t,stars, fo)
```

```
236     Save_snap2(i, t,stars)
237 
238     i = i+1
239 
240     if isfile("stop"):
241         break
242 
243 
244 grav.stop()
245 integrator.stop()
246 multiples_code.stop()
247 
```